

 Open access • Journal Article • DOI:10.1111/J.1365-3091.2011.01247.X

## **Depositional processes, bedform development and hybrid bed formation in rapidly decelerated cohesive (mud–sand) sediment flows — [Source link](#)**

Jaco H. Baas, James L. Best, Jeff Peakall

**Institutions:** Bangor University, University of Illinois at Urbana–Champaign, University of Leeds

**Published on:** 01 Dec 2011 - Sedimentology (Wiley)

**Topics:** Bedform, Plug flow, Silt, Turbulence and Flow velocity

Related papers:

- [Subaqueous sediment density flows: Depositional processes and deposit types](#)
- [Hybrid sediment gravity flow deposits – Classification, origin and significance](#)
- [A Phase Diagram for Turbulent, Transitional, and Laminar Clay Suspension Flows](#)
- ["Linked" debrites in sand-rich turbidite systems - origin and significance](#)
- [Deposits of flows transitional between turbidity current and debris flow](#)

Share this paper:    

View more about this paper here: <https://typeset.io/papers/depositional-processes-bedform-development-and-hybrid-bed-164ix5zmvi>



**Depositional Processes, Bedform Development and Hybrid  
Bed Formation in Rapidly Decelerated Cohesive (Mud-Sand)  
Sediment Flows**

Journal:	<i>Sedimentology</i>
Manuscript ID:	SED-2010-OM-137.R1
Manuscript Type:	Original Manuscript
Keywords:	Bedforms, Current ripples, Decelerating flows, Turbulence modulation, Bed shear strength, Cohesion, Clay suspensions, Hybrid beds

SCHOLARONE™  
Manuscripts

1  
2  
3  
4  
5  
6  
7  
8  
9  
10  
11  
12  
13  
14  
15  
16  
17  
18  
19  
20  
21  
22

# Depositional Processes, Bedform Development and Hybrid Bed Formation in Rapidly Decelerated Cohesive (Mud-Sand) Sediment Flows

23  
24  
25  
26

**JACO H. BAAS<sup>1</sup>, JAMES L. BEST<sup>2</sup> & JEFFREY PEAKALL<sup>3</sup>**

27  
28  
29  
30

*<sup>1</sup>School of Ocean Sciences, Bangor University, Menai Bridge LL59 5AB, Wales, United Kingdom*

31  
32  
33  
34  
35

*<sup>2</sup>Departments of Geology, Geography and Mechanical Science and Engineering and Ven Te Chow Hydrosystems Laboratory, University of Illinois at Urbana-Champaign, 1301 West Green Street, Urbana, Illinois 61801, U.S.A.*

36  
37  
38  
39

*<sup>3</sup>School of Earth and Environment, University of Leeds, Woodhouse Lane, Leeds LS2 9JT, United Kingdom*

40  
41  
42  
43  
44  
45  
46  
47  
48  
49  
50  
51

Running title: *Bedforms in decelerated cohesive flows*

52  
53  
54  
55  
56  
57  
58  
59  
60

*Keywords:* Bedforms; Current ripples; Flow deceleration; Turbulence modulation; Bed shear strength; Cohesion; Clay suspensions; Hybrid beds

**ABSTRACT**

Flows with high suspended sediment concentrations are common in many sedimentary environments, and their flow properties may show a transitional behaviour between fully turbulent and quasi-laminar plug flows. The characteristics of these transitional flows are a function of both clay concentration and type as well as the applied fluid stress. This paper investigates the behaviour of rapidly decelerated to steady flows that contain a mixture of sand, silt and clay, and explores the effect of different clay (kaolin) concentrations on the dynamics of flow over a mobile bed, and the bedforms and stratification produced. Experiments were conducted in a recirculating slurry flume capable of transporting high clay concentrations. Ultrasonic Doppler velocity profiling was used to measure the flow velocity within these concentrated suspension flows. The development of current ripples under decelerated flows of differing kaolin concentration was documented and evolution of their height, wavelength and migration rate quantified.

This work confirms past work over smooth, fixed beds, which showed that, as clay concentration rises, a distinct sequence of flow types is generated: turbulent flow (TF), turbulence-enhanced transitional flow (TETF), lower transitional plug flow (LTPF), upper transitional plug flow (UTPF) and a quasi-laminar plug flow (QLPF). Each of these flow types produces an initial flat bed upon rapid flow deceleration, followed by reworking of these deposits through the development of current ripples during the subsequent steady flow in TF, TETF and LTPF. The initial flat beds are structureless, but have diagnostic textural properties, caused by differential settling of sand, silt and cohesive mud, which forms characteristic bipartite beds that initially consist of sand overlain by silt or clay. As clay concentration in the formative flow increases, ripples first increase in mean height and wavelength under TETF and LTPF regimes, which is attributed to the additional turbulence generated under these flows that subsequently causes greater leeside erosion. As clay concentration increases further from a LTPF, ripples cease to exist under the UTPF and QLPF conditions investigated herein. This disappearance of ripples appears due to both turbulence suppression at higher clay concentrations, as well as the increasing shear strength of the bed sediment that becomes more difficult to erode as clay concentration increases. The stratification within the ripples formed after rapid deceleration of the transitional flows reflects the availability of sediment from the bipartite bed. The exact nature of the ripple cross-stratification in these flows is a direct function of the duration of the formative flow and the texture of the initial flat bed, and ripples do not form in cohesive flows with a Reynolds number smaller than  $\sim 12,000$ .

Examples are given of how the unique properties of the current ripples and plane beds, developing below decelerated transitional flows, could aid in the interpretation of depositional processes in modern and ancient sediments. This includes a new model for hybrid beds that explains their formation in terms of a combination of vertical grain-size segregation and longitudinal flow transformation.

## 1. INTRODUCTION

Sediment-laden flows of high density occur in most natural environments, and their depositional products may comprise a significant part of the sedimentary rock record. For instance, river channels may form the conduit of subaerial debris flows and hyperconcentrated flows, especially in mountainous regions where large volumes of weathered sediment are available (e.g. Van Maren *et al.*, 2009), whilst lahars are dense, and highly destructive, mixtures of sediment and water that move down the slopes of volcanoes (Pierson, 1985; Best, 1992). During storms combined with high rainfall in shallow marine environments, large quantities of sediment may be flushed out of estuaries onto the continental shelf by means of mobile fluid muds (e.g. "oceanic floods" of Traykovski *et al.* 2000). Flows of high density are probably most common on the continental slope and continental rise, where a large variety of sediment gravity flow deposits has been found in submarine fans, both in contemporary environments and in the geological record (e.g. Dasgupta, 2003). These deposits include turbidites, submarine debris flow deposits, slurry flow deposits, linked debrites-turbidites (i.e. hybrid event beds), and submarine slump and slide deposits (e.g. Mulder & Alexander, 2001; Haughton *et al.*, 2009). Despite their common occurrence, the interaction of high-density flows with their substrate and the formation of any diagnostic sedimentary structures are still poorly understood when compared to low-density flows. This is partly because only since the introduction of ultrasonic Doppler velocimetry profiling (Best *et al.*, 2001; Baas & Best, 2002) has it become possible to reveal the complex internal dynamics of flows in laboratory experiments that transport large amounts of sand, silt and clay.

The dynamics of high-density flows are unique, and recent work has shown that clearwater or low-density flows cannot be used as a surrogate for high-density flows (Mulder & Alexander, 2001; Baas & Best, 2002; Baas *et al.*, 2009), especially if these flows transport clay particles. Clay has cohesive properties, because electrostatic forces cause the particles to attract each other, thus forming clay flocs or gels (i.e., pervasive, volume-filling networks of bonded clay particles). These particle bonds can make a flow strong enough to modulate turbulence, or, if turbulent enough, a flow can break relatively weak clay flocs or clay gels into smaller constituents. This feedback between clay concentration and applied fluid stress controls not only the flow properties, but may also affect the exchange of sediment between bed and flow, and thus may be expected to have important implications for depositional properties. The present paper compares the depositional properties of low- and high-density flows by investigating the development of bedforms and their sedimentary structures across a wide range of suspended sediment concentrations, including turbulent, transitional and quasi-laminar flow phases (*sensu* Baas *et al.*, 2009). This approach is inspired by the fact that bedform analysis is an essential tool for modelling sediment transport in modern environments and reconstructing sedimentary processes from core and outcrop data.

Natural high-density flows often lose their sediment load quickly when the driving force is removed, such as by a reduction in slope angle or decrease in flow confinement. This may give rise to characteristic deposit shapes, such as the blunt frontal terminations of debris flow deposits

1  
2 (Amy *et al.*, 2005; Amy & Talling, 2006), and characteristic internal organisation, such as massive,  
3 “structureless”, sandstones (Stow & Johansson, 2000). In the present laboratory experiments,  
4 conditions of rapid depletion were simulated using open-channel suspension flows that were  
5 supersaturated with sediment and thus highly depositional. This produced unique bedforms, the  
6 form and size of which varied greatly, yet in a predictable manner, with suspended clay  
7 concentration. These geometrical variations were governed by processes of turbulence modulation  
8 and by differential settling of non-cohesive sand, silt and cohesive mud.  
9  
10  
11  
12  
13  
14  
15  
16

## 17 **2. TURBULENT, TRANSITIONAL AND QUASI-LAMINAR FLOWS**

18  
19  
20 Turbulence modulation in a flow laden with clay particles is dependent on the properties of both  
21 the fluid and the boundary over which the flow is moving. The properties of a turbulent flow may  
22 change as a function of fluid shear, clay type and clay concentration (i.e. viscosity and yield  
23 strength), bed surface roughness (including grain and bedform roughness) and distance from the  
24 sediment bed. The complex interaction of these parameters renders predictions of turbulence  
25 modulation a difficult task, and past experimental work has therefore taken a stepwise approach by  
26 investigating each parameter in isolation. Baas & Best (2002) and Baas *et al.* (2009) studied the  
27 flow of kaolin-laden fluids over a smooth, fixed, horizontal bed and revealed a distinct series of  
28 changes in the properties of turbulent flow as clay concentration and mean flow velocity were  
29 increased. Other laboratory experiments have focussed on the influence of grain roughness, by  
30 comparing the mean and turbulent flow properties of clay-rich flows moving over a smooth and  
31 rough (7 mm gravel) surface (Baas & Best, 2009), and on form drag in flows over a fixed, idealised  
32 current ripple (Baas & Best, 2008).  
33  
34  
35  
36  
37  
38  
39  
40

41 Baas *et al.* (2009) proposed a clay-flow phase diagram with five flow-phase stability fields (Fig.  
42 1). At the lowest suspended clay concentrations, a normal turbulent flow (TF) is present, with a  
43 standard logarithmic velocity profile and turbulence intensities that decrease away from the bed  
44 (Fig. 2). In the TF phase, turbulent fluctuations in flow velocity were inferred to be strong enough to  
45 prevent the clay from forming cohesive bonds, and the flow dynamics were similar to clearwater  
46 flows. At the highest clay concentrations, however, the clay particles formed a pervasive gel,  
47 making the flow viscous and suppressing most of the turbulence. This ‘quasi-laminar plug flow’  
48 (QLPF) is characterised by a rigid plug without internal deformation, i.e. the yield strength exceeds  
49 the shear stresses within the plug. The rigid plug moves on top of a weakly turbulent to laminar  
50 basal shear layer (Fig. 2). Between these two extremes, three types of ‘transitional flow’ were  
51 distinguished; with increasing clay concentration: turbulence-enhanced transitional flow (TETF);  
52 lower transitional plug flow (LTPF); and upper transitional plug flow (UTPF) (Fig. 1). TETF is  
53 characterised by enhanced turbulence intensity over the entire flow depth, with an internal shear  
54 layer just above the bed being inferred to be the source of this additional turbulence (Baas and  
55  
56  
57  
58  
59  
60

1  
2 Best, 2002; Baas *et al.*, 2009). This shear layer separates a lower, thickened viscous sublayer from  
3 the overriding flow. Vorticity, in the form of Kelvin-Helmholtz instabilities, penetrates upwards into  
4 the flow from the shear layer, whilst gradually dissipating (Fig. 2; Baas and Best, 2002). LTPF  
5 forms at higher clay concentrations than TETF, and is characterised by the formation of a plug  
6 flow region, which is virtually free of turbulence and has low, or no, vertical gradients in  
7 downstream velocity (Fig. 2). The plug flow forms first near the water surface, where shear is  
8 lowest, and expands downward as clay concentration is increased. However, turbulence  
9 enhancement, probably by the same process as in the TETF, persists near the bed in LTPF, thus  
10 maximising the gradient of turbulent intensity between the base and top of the flow (Fig. 2). At  
11 around the height of the internal shear layer in LTPF, the velocity time-series contains saw-tooth  
12 shaped velocity fluctuations with a periodicity of up to 10 s, which were also interpreted to be  
13 caused by Kelvin-Helmholtz instabilities (Fig. 2; Baas and Best, 2002; Baas *et al.*, 2009). UTPF  
14 is a flow intermediate between LTPF and QLPF (Fig. 1), in which the plug flow region thickens as  
15 clay concentration increases, whilst turbulence is attenuated along the entire flow depth, as  
16 turbulence forces are progressively outbalanced by viscosity and yield strength (i.e. cohesive  
17 forces) of the suspended clay (Fig. 2). Although the basal shear layer still exists in UTPF, it  
18 becomes a progressively weaker source of turbulence, until it ceases to produce turbulence  
19 altogether in QLPF.  
20  
21  
22  
23  
24  
25  
26  
27  
28  
29  
30

31 Baas & Best (2008) extended the work of Baas & Best (2002) by introducing kaolin-laden flows  
32 over a smooth, idealised, fixed current ripple, and investigated the dynamics of turbulent,  
33 transitional and laminar flow above and downstream of the ripple crest. With increasing suspended  
34 clay concentration, Baas & Best (2008) identified the following principal flow types: (1) Normal  
35 turbulent flow, dominated by flow separation downstream of the ripple crest; (2) Turbulence-  
36 enhanced transitional flow, which is analogous to the TETF and LTPF of Baas *et al.* (2009) (phase  
37 1 in Fig. 3), with increased turbulence intensities along the free shear layer of the separation zone,  
38 within the separation zone and at flow reattachment, and generally low turbulence levels in the free  
39 flow above the ripple due to the initial development of a plug flow; (3) Turbulence-attenuated  
40 transitional flows (phases 2 and 3 in Fig. 3, analogous to the UTPF of Baas *et al.*, 2009), in which  
41 strong cohesive forces dampen fluid turbulence within the entire separation zone and a thick plug  
42 flow develops in the free flow above the ripple; and (4) Laminar flow with full gelling, (Phase 4 in  
43 Fig. 3), which is characterised by the presence of a pronounced laminar plug flow, analogous to  
44 the QLPF of Baas *et al.* (2009), with a region of stagnant flow in the ripple lee. Furthermore, Baas  
45 & Best (2008) distinguished two phases of turbulence-attenuated transitional flow. At Phase-2 clay  
46 concentrations (Fig. 3), turbulence is attenuated within the separation zone, but the length of the  
47 separation zone is similar to that under turbulent flow and turbulence-enhanced transitional flows.  
48 However, in the highly concentrated turbulence-attenuated transitional flow (Phase 3 in Fig. 3), the  
49 separation zone shortens in length, and is associated with a further decrease in turbulence  
50 intensity. Baas & Best (2008) reasoned that the spatially-variable nature of turbulence production  
51  
52  
53  
54  
55  
56  
57  
58  
59  
60

1  
2 over a bedform influenced how the interactions between cohesive and turbulence forces affected  
3 the structure of clay flows at different locations across the ripple profile. Since the production of  
4 turbulence at the base of the ripple lee slope is low, Baas & Best (2008) argued that a stable gel  
5 thus forms at a lower clay concentration than in the free shear layer of the separation zone, where  
6 strong mixing occurs, and at flow reattachment, where instantaneous bed shear stresses are  
7 higher than anywhere else in the ripple trough. It can be hypothesised that these spatial  
8 differences in turbulence modulation will have important implications for the development and  
9 stability of bedforms in mobile sediment, and thus provide a potential mechanism for differences in  
10 bedform shape and size formed in transitional clay flows.

11  
12 Furthermore, the process of near-bed turbulence enhancement in the ripple lee increases the  
13 potential for bed erosion, and may therefore lead to an increase in the development rate and  
14 equilibrium size of natural bedforms (Baas & Best, 2008). Conversely, near-bed turbulence  
15 attenuation may reduce the potential for bed erosion, and cause bedforms to develop more slowly,  
16 and their equilibrium size to be smaller, than in turbulent flow. However, these speculations  
17 concerning transitional flow bedforms must be treated with caution, since the experiments of Baas  
18 & Best (2008) were limited in that they did not investigate mobile bedforms and hence were unable  
19 to erode the bed. Consequently, the possible effect of the infiltration of fine-grained material into  
20 the bed upon the mechanical properties of the bed (Packman & MacKay, 2003) and bedform  
21 development were not investigated.

22  
23 The new experimental results presented herein address these previous simplifications and  
24 analyse the formation of bedforms in mobile sediment, thus investigating another important  
25 variable that must be considered when developing more accurate predictions of the feedback  
26 mechanisms between sediment beds and both transitional and laminar clay flows in natural  
27 environments. It should be emphasised that the present experiments detail the formation of  
28 bedforms below rapidly decelerated open-channel flows laden with a mixture of sand, silt and clay,  
29 in which cohesive forces in the flows were at least as important as cohesive forces within the  
30 actively-forming sediment bed. This is in contrast to conditions that start with clear water and mixed  
31 sand-clay beds, in which bed cohesion may be expected to have the largest impact on bedform  
32 dynamics.

### 33 34 35 36 37 38 39 40 41 42 43 44 45 46 47 48 49 50 51 52 53 54 55 56 57 58 59 60

### 3. EXPERIMENTAL SETUP AND METHODOLOGY

14  
15  
16  
17  
18  
19  
20  
21  
22  
23  
24  
25  
26  
27  
28  
29  
30  
31  
32  
33  
34  
35  
36  
37  
38  
39  
40  
41  
42  
43  
44  
45  
46  
47  
48  
49  
50  
51  
52  
53  
54  
55  
56  
57  
58  
59  
60  
61  
62  
63  
64  
65  
66  
67  
68  
69  
70  
71  
72  
73  
74  
75  
76  
77  
78  
79  
80  
81  
82  
83  
84  
85  
86  
87  
88  
89  
90  
91  
92  
93  
94  
95  
96  
97  
98  
99  
100  
101  
102  
103  
104  
105  
106  
107  
108  
109  
110  
111  
112  
113  
114  
115  
116  
117  
118  
119  
120  
121  
122  
123  
124  
125  
126  
127  
128  
129  
130  
131  
132  
133  
134  
135  
136  
137  
138  
139  
140  
141  
142  
143  
144  
145  
146  
147  
148  
149  
150  
151  
152  
153  
154  
155  
156  
157  
158  
159  
160  
161  
162  
163  
164  
165  
166  
167  
168  
169  
170  
171  
172  
173  
174  
175  
176  
177  
178  
179  
180  
181  
182  
183  
184  
185  
186  
187  
188  
189  
190  
191  
192  
193  
194  
195  
196  
197  
198  
199  
200  
201  
202  
203  
204  
205  
206  
207  
208  
209  
210  
211  
212  
213  
214  
215  
216  
217  
218  
219  
220  
221  
222  
223  
224  
225  
226  
227  
228  
229  
230  
231  
232  
233  
234  
235  
236  
237  
238  
239  
240  
241  
242  
243  
244  
245  
246  
247  
248  
249  
250  
251  
252  
253  
254  
255  
256  
257  
258  
259  
260  
261  
262  
263  
264  
265  
266  
267  
268  
269  
270  
271  
272  
273  
274  
275  
276  
277  
278  
279  
280  
281  
282  
283  
284  
285  
286  
287  
288  
289  
290  
291  
292  
293  
294  
295  
296  
297  
298  
299  
300  
301  
302  
303  
304  
305  
306  
307  
308  
309  
310  
311  
312  
313  
314  
315  
316  
317  
318  
319  
320  
321  
322  
323  
324  
325  
326  
327  
328  
329  
330  
331  
332  
333  
334  
335  
336  
337  
338  
339  
340  
341  
342  
343  
344  
345  
346  
347  
348  
349  
350  
351  
352  
353  
354  
355  
356  
357  
358  
359  
360  
361  
362  
363  
364  
365  
366  
367  
368  
369  
370  
371  
372  
373  
374  
375  
376  
377  
378  
379  
380  
381  
382  
383  
384  
385  
386  
387  
388  
389  
390  
391  
392  
393  
394  
395  
396  
397  
398  
399  
400  
401  
402  
403  
404  
405  
406  
407  
408  
409  
410  
411  
412  
413  
414  
415  
416  
417  
418  
419  
420  
421  
422  
423  
424  
425  
426  
427  
428  
429  
430  
431  
432  
433  
434  
435  
436  
437  
438  
439  
440  
441  
442  
443  
444  
445  
446  
447  
448  
449  
450  
451  
452  
453  
454  
455  
456  
457  
458  
459  
460  
461  
462  
463  
464  
465  
466  
467  
468  
469  
470  
471  
472  
473  
474  
475  
476  
477  
478  
479  
480  
481  
482  
483  
484  
485  
486  
487  
488  
489  
490  
491  
492  
493  
494  
495  
496  
497  
498  
499  
500  
501  
502  
503  
504  
505  
506  
507  
508  
509  
510  
511  
512  
513  
514  
515  
516  
517  
518  
519  
520  
521  
522  
523  
524  
525  
526  
527  
528  
529  
530  
531  
532  
533  
534  
535  
536  
537  
538  
539  
540  
541  
542  
543  
544  
545  
546  
547  
548  
549  
550  
551  
552  
553  
554  
555  
556  
557  
558  
559  
560  
561  
562  
563  
564  
565  
566  
567  
568  
569  
570  
571  
572  
573  
574  
575  
576  
577  
578  
579  
580  
581  
582  
583  
584  
585  
586  
587  
588  
589  
590  
591  
592  
593  
594  
595  
596  
597  
598  
599  
600  
601  
602  
603  
604  
605  
606  
607  
608  
609  
610  
611  
612  
613  
614  
615  
616  
617  
618  
619  
620  
621  
622  
623  
624  
625  
626  
627  
628  
629  
630  
631  
632  
633  
634  
635  
636  
637  
638  
639  
640  
641  
642  
643  
644  
645  
646  
647  
648  
649  
650  
651  
652  
653  
654  
655  
656  
657  
658  
659  
660  
661  
662  
663  
664  
665  
666  
667  
668  
669  
670  
671  
672  
673  
674  
675  
676  
677  
678  
679  
680  
681  
682  
683  
684  
685  
686  
687  
688  
689  
690  
691  
692  
693  
694  
695  
696  
697  
698  
699  
700  
701  
702  
703  
704  
705  
706  
707  
708  
709  
710  
711  
712  
713  
714  
715  
716  
717  
718  
719  
720  
721  
722  
723  
724  
725  
726  
727  
728  
729  
730  
731  
732  
733  
734  
735  
736  
737  
738  
739  
740  
741  
742  
743  
744  
745  
746  
747  
748  
749  
750  
751  
752  
753  
754  
755  
756  
757  
758  
759  
760  
761  
762  
763  
764  
765  
766  
767  
768  
769  
770  
771  
772  
773  
774  
775  
776  
777  
778  
779  
780  
781  
782  
783  
784  
785  
786  
787  
788  
789  
790  
791  
792  
793  
794  
795  
796  
797  
798  
799  
800  
801  
802  
803  
804  
805  
806  
807  
808  
809  
810  
811  
812  
813  
814  
815  
816  
817  
818  
819  
820  
821  
822  
823  
824  
825  
826  
827  
828  
829  
830  
831  
832  
833  
834  
835  
836  
837  
838  
839  
840  
841  
842  
843  
844  
845  
846  
847  
848  
849  
850  
851  
852  
853  
854  
855  
856  
857  
858  
859  
860  
861  
862  
863  
864  
865  
866  
867  
868  
869  
870  
871  
872  
873  
874  
875  
876  
877  
878  
879  
880  
881  
882  
883  
884  
885  
886  
887  
888  
889  
890  
891  
892  
893  
894  
895  
896  
897  
898  
899  
900  
901  
902  
903  
904  
905  
906  
907  
908  
909  
910  
911  
912  
913  
914  
915  
916  
917  
918  
919  
920  
921  
922  
923  
924  
925  
926  
927  
928  
929  
930  
931  
932  
933  
934  
935  
936  
937  
938  
939  
940  
941  
942  
943  
944  
945  
946  
947  
948  
949  
950  
951  
952  
953  
954  
955  
956  
957  
958  
959  
960  
961  
962  
963  
964  
965  
966  
967  
968  
969  
970  
971  
972  
973  
974  
975  
976  
977  
978  
979  
980  
981  
982  
983  
984  
985  
986  
987  
988  
989  
990  
991  
992  
993  
994  
995  
996  
997  
998  
999  
1000

Fourteen laboratory experiments were conducted using an 8.75 m long and 0.3 m wide slurry flume in the Sorby Environmental Fluid Dynamics Laboratory, University of Leeds (Table 1; Fig. 4). A range of mixtures of fresh water, cohesive clay and non-cohesive silt and sand were circulated through the flume by means of a variable-discharge slurry pump with an open, centrifugal screw mechanism (Fig. 4) that produced minimal flow disturbance. The exception was Run 1, which was



1 a control experiment with non-cohesive sediment only. The cohesive clay used in the experiments  
2 was kaolin with a median diameter,  $D_{50}$ , of 0.0073 mm, whilst the non-cohesive sediment had a  
3 bimodal grain-size distribution with a median diameter of 0.084 mm and modal sizes of 0.048 mm  
4 and 0.300 mm (Fig. 5). At the upstream end of the flume, in order to straighten flow at the inlet and  
5 dampen any inlet turbulence, all flows moved underneath a wooden board set flush with the water  
6 surface, through a grid and then through a horizontal stack of pipes (Fig. 4). Downstream of the  
7 pipe stack, the flows moved over a fixed bed of medium-sized gravel along the entire length of the  
8 flume. The mean roughness height of the gravel bed was  $\sim 8$  mm. Turbulence production over the  
9 gravel bed was sufficient to keep most sand, silt and clay particles in suspension at high flow  
10 discharge ( $\sim 50 \text{ L s}^{-1}$ , equivalent to a mean flow velocity of  $1.2 \text{ m s}^{-1}$ ), and thus allowed simulation  
11 of a steady-state suspension flow at the start of each experiment. At the start of each run, once the  
12 flows had been recirculated at  $50 \text{ L s}^{-1}$  for several minutes, the discharge was reduced  
13 instantaneously to  $\sim 19 \text{ L s}^{-1}$  (equivalent to a flow velocity of  $\sim 0.46 \text{ m s}^{-1}$  at a flow depth of 0.15 m),  
14 thus producing a supersaturated suspension load. The sediment that was deposited from the  
15 suspension formed a horizontal bed on which bedform development could take place. This  
16 sediment settled quickly and covered the gravel surface so that the underlying gravel clasts did not  
17 influence subsequent bedform development in the sand-silt-clay mixture.

18 The development of the bed was monitored through the sidewall of the flume using digital  
19 photographs, line drawings and detailed descriptions of the sedimentological properties of the bed.  
20 The height and wavelength of the bedforms was tracked, with each individual bedform being  
21 numbered to allow calculation of bedform migration rates. Ultrasonic Doppler velocimetry profiling  
22 (UDVP; Best *et al.*, 2001; Baas and Best, 2002, 2008) was used to measure the downstream  
23 component of flow velocity at seven or more different heights above the sediment bed near the end  
24 of each run. Additional velocity time-series were collected at the start and middle of selected runs.  
25 UDVP quantifies flow velocity by determining the Doppler shift in ultrasound frequency as small  
26 particles pass through a measurement volume; these probes are particularly well-suited for  
27 measuring velocities in opaque suspensions (Takeda, 1991; Best *et al.*, 2001; Baas and Best,  
28 2002). The present experiments used 4 MHz UDVP probes, of 8 mm diameter that acquired  
29 simultaneous velocity data along a profile of up to 128 points along the axis of the ultrasound  
30 beam, which in the present experiments extended up to 0.105 m from the probe head. No  
31 velocities were recorded in the proximal 0.012 m of each profile, where the stagnation of flow by  
32 the probes was found to be unacceptably large. The UDVP probes collected velocity data for a  
33 duration of 75-87 s at a temporal resolution of 115-133 Hz.

34 The temporal mean flow velocity,  $\bar{U}$ , and its root-mean square,  $RMS(u')$ , which approximates  
35 the horizontal component of turbulence intensity, were calculated from the time-series of  
36 instantaneous velocity data at each measurement location:  
37  
38  
39  
40  
41  
42  
43  
44  
45  
46  
47  
48  
49  
50  
51  
52  
53  
54  
55  
56  
57  
58  
59  
60

$$\bar{U} = \frac{1}{n} \sum_{i=1}^n u_i \quad (1)$$

$$RMS(u') = \sqrt{\frac{1}{n} \sum_{i=1}^n (u_i - \bar{U})^2}$$

where  $n$  is the number of velocity measurements. For turbulent and low-density transitional flows, the depth-averaged flow velocity,  $\bar{U}$ , was computed using a curve-fitting procedure based on the logarithmic law for wall-bounded shear flows (e.g. Van Rijn, 1990):

$$\bar{U} = \frac{1}{h - z_0} \int_{z_0}^h \frac{u_*}{\kappa} \ln\left(\frac{z}{z_0}\right) dz \quad (2)$$

where  $u_*$  is the shear velocity,  $\kappa$  is the von Kármán constant ( $\kappa=0.4$ ),  $h$  is the flow depth,  $z$  is height above the bed, and  $z_0$  is the reference height at which  $\bar{U}=0$ . Equation 2 cannot be used for clay flows with strongly modulated turbulence, because the velocity profile of these flows deviates from a logarithmic curve. Instead,  $\bar{U}$ -values for laminar and high-density transitional flows were calculated using the Coles wake function (Coles, 1956; Wang & Plate, 1996; Wang *et al.* 2001):

$$\bar{U} = \frac{1}{h - z_0} \int_{z_0}^h \left( \bar{U}_{\max} - \frac{u_*}{\kappa} \ln\left(\frac{h}{z}\right) - \frac{2Wu_*}{\kappa} \cos^2\left(\frac{\pi z}{2h}\right) \right) dz \quad (3)$$

where  $\bar{U}_{\max}$  is the maximum value of temporal mean velocity and  $W$  is the wake strength coefficient. In Eq. 3, the von Kármán constant is assumed independent of clay concentration. In the present study, the depth-averaged velocity was between 0.35 and 0.55 m s<sup>-1</sup> (Table 1), flow depths were ~0.15 m, shear velocities ranged from 0.02 m s<sup>-1</sup> to 0.09 m s<sup>-1</sup>, and the wake strength coefficient ranged from -0.9 to +0.5.

Siphon tubes connected to peristaltic pumps were used to collect suspension samples to determine the volumetric sediment concentration (Fig. 4) through standard weighing and drying. The suspended sediment concentration,  $C_o$ , was measured near the bed ~1 minute after flow deceleration. Mean suspended sediment concentration,  $C_e$ , was calculated from siphon data at six different heights above the bed near the end of the each run, at  $t=2.3$  h. The pre-deceleration concentration of non-cohesive sediment within the flows was constant at ~3%, which is well below the Bagnold limit of 9% (Bagnold, 1954); this limit is widely regarded as the threshold for turbulence modulation in non-cohesive sand- and silt-laden flows (e.g., Mulder and Cochoonat, 1996). Volumetric kaolin concentrations were between 0.2% and 19.2% (i.e., between 5 g L<sup>-1</sup> and 500 g L<sup>-1</sup>), encompassing the flow phases where turbulence modulation and full turbulence suppression are expected (Baas *et al.*, 2009). Due to the unstable nature of the bedforms in clay-rich flows (see *Results*), it was impossible to collect bed samples for grain-size analysis.

The Froude number,  $Fr$ , and flow Reynolds number,  $Re$ , were calculated to express the basic flow data in dimensionless form:

$$Fr = \frac{\overline{U}}{\sqrt{gh}} \quad (4)$$

$$Re = \frac{\overline{U}z_p\rho}{\eta} \quad (5)$$

where  $g$  is acceleration due to gravity,  $\rho$  is flow density,  $\eta$  is dynamic viscosity of the flow, and  $z_p$  is the thickness of the flow region between the base of the plug flow and the sediment surface. As reasoned in Baas *et al.* (2009),  $z_p$  is used in Eq. 5 instead of flow depth, because the largest length scales of turbulence within the transitional and laminar clay flows are limited by the distance between the bed and the base of the plug-flow region. In turbulent flows and turbulence-enhanced transitional flows, in which plug-flow regions are absent, the length scale in Eq. 5 is equal to the flow depth (i.e.  $z_p=h$ ). Following Wan (1982), the dynamic viscosity,  $\eta$ , and yield strength,  $\tau_y$ , of the suspensions were approximated from the measured suspended-sediment concentrations as:

$$\eta = 0.001 + 0.206 \left( \frac{C_0}{100} \right)^{1.68} \quad (6)$$

$$\tau_y = 1280 \left( \frac{C_0}{100} \right)^3 \quad (7)$$

Equations 6 and 7 are valid only for kaolin.

The measured bedform data were processed using the methodology proposed by Baas (1994, 1999), with the development of bedform height and wavelength being quantified using the best-fit equations:

$$\frac{H_t}{H_e} = 1 - (0.01)^{\frac{t}{T_e(H)}} \quad (8)$$

$$\frac{L_t - L_0}{L_e - L_0} = 1 - (0.01)^{\frac{t}{T_e(L)}} \quad (9)$$

where  $H_t$  and  $L_t$  are bedform height and wavelength at time  $t$ ,  $H_e$  and  $L_e$  are the equilibrium height and wavelength,  $L_0$  is the wavelength of the first bedforms appearing on the flat bed, and  $T_e(H)$  and  $T_e(L)$  are the equilibrium time for height and wavelength, respectively. Following Baas (1994, 1999), the equilibrium time was defined as the time required to reach 99% of the equilibrium bedform height and wavelength. Bedform heights were found to reach equilibrium values well before bedform wavelengths (cf. Baas, 1994, 1999), but part of this difference was caused by inaccuracies in predicting  $T_e(L)$ - and  $L_e$ -values due to the fact that some of the experiments were not continued long enough into the stage of fully developed bedforms. This limitation was not a problem for the  $T_e(H)$ - and  $H_e$ -data. Therefore, the analysis presented herein uses comparison of wavelength values for mean wavelength values at  $t > 1$  h only, and for bedform height this method is used in addition to the equilibrium values for height from Eq. 9.

The mean bedform migration rates were converted to a bed sediment flux in order to compare differences in sediment transport rate due to bedform movement below rapidly decelerated turbulent, transitional and quasi-laminar flows using (Van Den Berg, 1987):

$$q_b = \beta(1 - p)H_e\bar{u}_c \quad (10)$$

where  $q_b$  is the bed sediment flux per unit width,  $p$  is bed porosity ( $p=0.35$ ), and  $\bar{u}_c$  is mean bedform migration rate for  $t > 1$  h.  $\beta$  is 0.5 for triangular, sandy bedforms, and 0.6 for natural, sandy bedforms (Van Den Berg, 1987), but these values do not necessarily apply to bedforms in cohesive sediment. Therefore,  $\beta$  was measured for three randomly chosen bedforms, at the end of Runs 1 to 7, which showed that  $\beta$  increased with increasing initial clay concentration from 0.55 to 0.63 (Fig. 6).

## 4. RESULTS

### 4.1. Flow dynamics

The experiments covered the entire range of flow conditions previously documented by Baas *et al.* (2009) from turbulent via transitional to quasi-laminar flow at various suspended sediment concentrations and depth-averaged flow velocities (Table 1). The vertical profiles of  $\bar{U}$  and  $RMS(u')$  correspond well with the profiles expected from their position in the  $Re-Fr$  phase diagram of Baas *et al.* (2009) (Fig. 1). Run 1, with the lowest clay concentration, produced a 'classic' turbulent flow (TF) with a logarithmic velocity profile and upward-decreasing turbulence intensity (Fig. 7). Runs 2 to 5 were turbulence-enhanced transitional flows (TETF), with  $RMS(u')$  values up to 13% higher than in Run 1 (e.g. Run 3 in Fig. 7). These TETFs transported between 1.1% and 5.1% suspended sediment (Table 1).

At  $C_0=6.9\%$  and  $C_0=8.0\%$ , Runs 6 and 7 represent lower transitional plug flows (LTPF) with characteristically high  $RMS(u')$  near the bed (e.g. Run 6 in Fig. 7) and development of a plug flow region near the flow surface (Fig. 8). Figure 8 illustrates that the near-bed  $RMS(u')$  values increase from the beginning to end of both LTPF experiments. Moreover, it can be seen that a thin plug flow is present above  $z=100$  mm ( $z/h = 0.67$ ) at  $t=0.17$  h and  $t=1$  h in Run 7, but that a clear vertical velocity gradient has appeared at the same heights after 2 hours. Additionally, the velocity time series of Run 7 clearly changes with time (Fig. 9). At  $\sim 6$  mm above the bed, the time series shows distinct saw-tooth shaped velocity fluctuations at  $t=0.17$  h (cf. Fig. 2), and to a lesser degree at  $t=1$  h, but no such fluctuations are present at  $t=2$  h (Fig. 9). These observations suggest that both LTPFs become more turbulent in time, and hence move towards higher Reynolds numbers in the clay flow phase diagram.

1  
2 Run 8, which transported 10.1% sediment, is the only experiment that produced an upper  
3 transitional plug flow (UTPF), in which a pronounced plug flow region, moving on top of a layer with  
4 reduced turbulence, is apparent from the  $RMS(u')$  profiles (Fig. 7). At suspended sediment  
5 concentrations of  $\geq 12.1\%$ , the turbulence intensities are generally low and the plug flow region is  
6 well-developed (e.g. Run 12 in Fig. 7), showing the characteristics of quasi-laminar plug flows  
7 (QLPF).  
8  
9

#### 10 11 12 13 **4.2 Suspension settling phase** 14 15

16  
17 In all experiments, sediment settled rapidly onto the gravel surface directly after the flows were  
18 forced to decelerate. Although the resulting deposits were massive, structureless, and had a flat,  
19 horizontal surface, their texture changed as the initial suspended sediment concentration was  
20 increased. Both the TF and TETFs produced bipartite deposits, consisting of a sandy layer with a  
21 thickness of  $\sim 9$  mm that was overlain by a silty layer of thickness  $\sim 5$  mm (Fig. 10). Sandy layers of  
22 similar thickness were formed also from the decelerated LTPFs and UTPF, but the upper part of  
23 these deposits was different. In Run 6 (LTPF), a 7 mm thick muddy, rather than silty, layer  
24 developed that consisted of a mixture of silt-sized glass beads and kaolin clay. This layer had the  
25 appearance of a fluid mud, with a high water content and high mobility. As the suspended  
26 sediment concentration was increased, the thickness of the fluid mud layer increased to 23 mm in  
27 the UTPF (Run 8), and its thickness remained between 26 and 34 mm up to  $C_0=19.2\%$  (Run 14,  
28 QLPF). The thickness of the sand layer decreased with increasing sediment concentration for the  
29 QLPFs, until at  $C_0=16.5\%$  a basal sand no longer formed (Fig. 10); the sand grains were still  
30 present but floating in the fluid mud. At relatively low concentrations ( $C_0\sim 11\%$ ) in the QLPFs, sand  
31 grains visibly moved downward through the fluid mud at a significantly lower rate than in clear  
32 water. The fluid mud appeared particularly sandy in Runs 9 to 12 ( $12.1\% < C_0 < 16.5\%$ ). Plots of the  
33 development of bed thickness for selected high-concentration flows ((UTPF and QLPF; Fig. 11)  
34 show that the rate of deposition after flow deceleration ( $t=0$ ) increased as suspended sediment  
35 concentration was increased. Each curve shows rapid development of the bed thickness at  $t < 1$  h,  
36 with the rate of thickness increase becoming higher at greater sediment concentrations, but with  
37 the rate of development slowing at  $t > 1$  h.  
38  
39  
40  
41  
42  
43  
44  
45  
46  
47  
48  
49  
50

#### 51 52 **4.3 Bedform development phase** 53 54

55  
56 Bedform development commenced by reworking of the earlier formed bipartite flat bed in the TF,  
57 TETFs and LTPFs (Runs 1-7,  $C_0 \leq 8\%$ ), but in the UTPF and QLPFs no bedforms were generated,  
58 and the fluid-mud dominated beds remained until the end of each experiment (cf. Fig. 11). All the  
59 bedforms observed were classified as current ripples, since their height and wavelength were  
60 smaller than 60 mm and 600 mm, respectively (Ashley 1990). Figure 12 shows images of the

1  
2 longitudinal ripple profiles through the flume sidewall in flows with different suspended sediment  
3 concentration ( $C_0=0.2\%-8.0\%$ , Runs 1, 4, 6 and 7).  
4

5 The current ripples formed in turbulent flow (Run 1) were asymmetrical in vertical cross-section  
6 parallel to the main flow (Fig. 12), with well-developed flow separation being evident at the crest  
7 and reverse flow occurring in the ripple trough. As predicted from earlier work (e.g. Baas 1994,  
8 1999), the ripples started to grow at a high rate that then decreased until the equilibrium ripple  
9 dimensions were established, thus yielding the typical asymptotic development curves for ripple  
10 height and wavelength (Fig. 13). Equilibrium height and wavelength of the bedforms in Run 1 were  
11 13 mm (or 12.9 mm, if based on Eq. 8) and 110 mm, respectively, and the equilibrium height was  
12 reached at  $t=0.55$  h. The mean migration rate of current ripples in the TF was  $0.24 \text{ mm s}^{-1}$ .  
13  
14  
15  
16  
17

18 The internal structure of the developing ripples in TF of Run 1 was clearly influenced by the  
19 bipartite nature of the initial deposit ( $t_0$ , Fig. 14). The first small ripples that appeared on the bed  
20 were composed entirely of silt-sized sediment ( $t_1$ , Fig. 14), and bedform growth was controlled  
21 mainly by scour in the region of flow reattachment. When the depth of this scour reached the top  
22 of the sand layer, the sand grains were then entrained and transported to the downstream ripple  
23 crest. This sand accumulated in the crestal region for a short period of time ( $t_2$ , Fig. 14) before  
24 avalanching down the slip face. Silt-sized sediment was also transported along the ripple stoss  
25 side and then deposited in the ripple leeside. This process of sand layer scour after initial formation  
26 of the ripple produced silty and sandy foreset laminae that were clearly separated at this stage of  
27 ripple development, producing a rhythmic alternation in grain size within the cross-sets ( $t_3$ , Fig. 14)  
28 without any fluctuations in the flow velocity. However, at a later stage, when the bedform had  
29 migrated over a distance of approximately one ripple wavelength, the sediment became  
30 progressively more mixed and the foresets adopted a more uniform composition, becoming less  
31 distinct in their grain size differentiation ( $t_4$ , Fig. 14).  
32  
33  
34  
35  
36  
37  
38  
39  
40

41 The current ripples in the TETFs possessed an asymmetric form and asymptotic development  
42 curves similar to the ripples in the TF, but close inspection of the bedform data also revealed clear  
43 differences. As suspended sediment concentration was increased in the TETFs, the equilibrium  
44 height and wavelength of the ripples increased, which was closely matched by increases in  
45  $RMS(u')$  (Figs 15a-b and 15d). The first ripples appeared within several minutes of initial flow  
46 deceleration, except for Run 5, in which a delay of 5 minutes was observed. Equilibrium ripple  
47 development times for the TETFs varied from 0.5 to 1.5 h. The bed sediment flux in the TETFs  
48 decreased with increasing sediment concentration (Fig. 15c), again except for Run 5 ( $C_0=5.1\%$ ;  
49 Fig. 15c). In Run 5, a trend of increasing bed sediment flux commenced, which continued into the  
50 LTPF regime (Fig. 15c). Although recirculation in the leeside separation zone in the TETFs  
51 appeared visibly stronger than in the TF, this did not result in any change in internal sedimentary  
52 structure, and the temporal development of ripples shown in Fig. 14 also applies to the TETFs.  
53  
54  
55  
56  
57  
58  
59  
60 Simons *et al.* (1963) also found that ripple and dune wavelength increased as more bentonite was  
added to the flow, but that the ripple crests became more rounded as clay concentration increased.

1  
2 The increase in ripple size at higher suspended sediment concentrations continued into the  
3 LTPF regime, culminating in a 41% increase in equilibrium ripple height and an 85% increase in  
4 equilibrium ripple wavelength compared to the turbulent flow (at  $C_0=8.0\%$ , Fig. 15a-b). The largest  
5 ripple sizes in Run 7 coincide with maximum near-bed  $RMS(u')$  values in the same run (Fig. 15d).  
6 Although both LTPFs showed asymptotic ripple development curves (Fig. 13), there was a  
7 considerable delay in the first appearance of bedforms on the initially flat bed. This delay was 0.25  
8 h in Run 6 ( $C_0=6.9\%$ ), yet equilibrium height and wavelength were reached well before the end of  
9 the experiment. In contrast, equilibrium dimensions may not have been established by the end of  
10 Run 7 ( $C_0=8.0\%$ ), due to the delayed initiation of bedforms until  $t=1.7$  h (Fig. 13). The ripple height  
11 and wavelength for this experiment, shown in Fig. 15a-b, should therefore be regarded as  
12 minimum values. The bed sediment flux in Run 6 ( $C_0=6.9\%$ ) exhibits a local maximum (Fig. 15c),  
13 before dropping dramatically as suspended sediment concentration was increased towards the  
14 upper limit of bedform formation (Fig. 15c).

15 The temporal development of sedimentary structures depicted in Fig. 14 was most pronounced  
16 in the LTPFs, but bedform development in these flows was also visibly affected by the presence of  
17 fluid mud and strong vorticity in the ripple troughs. In these ripples, reverse flow within the leeside  
18 separation zone was strong enough to form prominent backflow ripples on the lower 20% of the  
19 slip face (Fig. 16a), which were  $\sim 5$  mm high and composed of muddy sediment. Avalanching of  
20 sandier sediment onto the upper 80% of the slip face led to burial of the backflow ripples, ultimately  
21 resulting in preservation of a relatively fine-grained layer with a serrated top surface that lay  
22 beneath the silty/muddy sand of the main bedform (Fig. 16a). The cohesive nature of the fluid mud  
23 in the bipartite beds of Run 7 ( $C_0=8.0\%$ ) was particularly clear from the steeply-dipping stoss sides  
24 of the ripples close to the leeside scour of the upstream bedforms (Fig. 16b,c). Moreover, muddy  
25 sand and sandy mud was found to drape the irregularly eroded layer of fluid mud in such a way  
26 that an asymmetric ripple profile was established (Fig. 16c). Usually, the muddy sand was stored in  
27 the upper part of the foresets, while the lower parts consisted of sandy mud (Fig. 16c). These  
28 textural and structural properties were typical of the ripples formed at  $t=2.5$  h in Run 7, which  
29 evolved from ripples with an elongate, convex upward layer of muddy sand on top of the firm mud  
30 layer (Fig. 16b;  $t=1.08$  h). This muddy sand contained low-angle cross-laminae, while the  
31 underlying mud was structureless, except for sub-vertical fluid escape structures (Fig. 16b).

## 54 5. INTERPRETATION

### 57 5.1 General

58 The experimental results presented herein demonstrate that bed development below rapidly  
59 waned sediment-laden flows is highly dependent on the cohesive and turbulence forces within the  
60

1  
2 flow and the textural and rheological properties of the bed. Baas & Best (2008) and Baas *et al.*  
3 (2009) have proposed that the balance between cohesive and turbulence forces controls the  
4 dynamic properties of clay-rich flows, with cohesive forces increasing at greater suspended clay  
5 concentrations due to the electrostatic bonding of electrically-charged clay minerals. At low clay  
6 concentrations, turbulence forces generated by shear at the bed-flow interface, and by shear within  
7 the flow, are capable of breaking these bonds, but as clay concentration is increased, the bonds  
8 eventually become sufficiently strong and spatially-extensive to attenuate turbulence. Turbulence  
9 attenuation starts near the top of the flow, where turbulence intensity is lowest, and progressively  
10 moves downward with increasing clay concentration, thus forming the plug flows found in flows  
11 with >5% suspended sediment (Fig. 7).

12  
13 The addition of cohesive clay to a non-cohesive sand or silt bed has been found to increase the  
14 critical shear stress for sediment entrainment by a factor of up to five (Mitchener & Torfs, 1996). A  
15 dramatic increase in sediment shear strength, and thus decrease in erodibility, is also inferred to  
16 have been important for the changing flow dynamics in the present experiments. Such changes not  
17 only occur from one experimental run to the next (Fig. 15), but also within individual runs, as  
18 exemplified by the temporal change of  $RMS(u')$  profiles within LTPFs (Fig. 8). Furthermore, it is  
19 essential to consider changes in the feedback mechanisms between the flow and sediment bed, as  
20 a result of changing surface drag and form roughness when ripples develop upon the bed.

## 31 32 33 **5.2 Suspension settling phase**

34  
35 After instantaneous flow deceleration from  $\sim 50 \text{ L s}^{-1}$  to  $19 \text{ L s}^{-1}$ , each flow formed a massive,  
36 structureless bed through settling of suspended sediment, thereby generating a flat horizontal  
37 surface, but the textural properties of these deposits changed as the initial volume of suspended  
38 clay particles increased, particularly in the LTPFs, UTPF and QLPFs. Differences in the settling  
39 velocity of the sand and silt particles account for the formation of the bipartite beds in flows  
40 carrying up to 5% suspended sediment (Fig. 10). The vast majority of kaolin remained in  
41 suspension in the TETFs, although some clay may potentially have settled with the sand and silt or  
42 infiltrated into the pore space between the silt and sand grains after deposition. The increased  
43 turbulence intensity in the TETFs had no apparent effect on the thickness of the initial sediment  
44 bed, suggesting that these flows possessed insufficient turbulence to maintain the sand and silt in  
45 suspension. The absence of stratification in the bipartite deposits also attests to rapid  
46 sedimentation from waned flows (Middleton, 1967; Arnott & Hand, 1989).

47  
48 The bipartite beds below the LTPFs also possessed a basal sand layer, but the upper part of  
49 these beds consisted of fluid mud rather than silt. This mud consisted of a mixture of kaolin clay  
50 and silt-sized particles, and the fluid mud layer began to form immediately after flow deceleration.  
51 The fact that these LTPFs are unable to keep all clay particles in suspension can be explained by  
52 vertical gradients in the balance between cohesive and turbulence forces. In the upper region of  
53  
54  
55  
56  
57  
58  
59  
60



1  
2 the flows, cohesive forces are strong enough to attenuate turbulence, particularly at  $C_0=8.0\%$  in  
3 Run 7 (Fig. 8), thus leading to a reduction in the turbulence support of silt and clay particles. Such  
4 a reduction in particle support is not compensated by an increase in cohesive matrix strength,  
5 because the yield strength is too low (Table 1), and therefore the silt and some clay settle out of  
6 the flow. This settling process occurs despite the particles having to fall through the lower region of  
7 the flow, where turbulence forces are strong and outbalance cohesive forces. However, after  
8 entering the lower region, it is difficult for the particles to be transported back upwards, because  
9 the LTPFs are strongly stratified and upward mixing is limited to the dissipation of more and more  
10 isolated vortices as clay concentration increases (Baas & Best, 2002). In time, progressively more  
11 mud accumulates in the lower region of the flow until the concentration is sufficiently high to form a  
12 fluid mud on top of the basal sand. The settling of clay into the lower flow region, and therefore the  
13 growth of the fluid mud layer, thus appears to be self-limiting, because turbulence gradually re-  
14 establishes itself upon removal of clay from the upper flow region, as shown by the increase in  
15  $RMS(u')$  in the upper half of LTPF of Run 7 from  $t=0.17$  h to  $t=2$  h (Fig. 8).

16  
17  
18  
19  
20  
21  
22  
23  
24  
25 Early deposition from the UTPF (Run 8,  $C_0=10.1\%$ ) occurs in a similar manner to the LTPFs,  
26 with sand grains segregating from the finer particles, but within the fine fraction the silt and clay are  
27 mixed and form a highly mobile layer of fluid mud. However, the fluid mud layer is considerably  
28 thicker than in the LTPFs (Fig. 10), which may be attributed to: (1) the greater availability of kaolin  
29 clay, since the initial sediment concentration is higher and the turbulence-attenuated plug flow  
30 layer is thicker (Fig. 7) than in the LTPFs; and (2) the drastically reduced near-bed turbulence  
31 intensity (Fig. 15d). In the UTPF it thus appears that turbulence forces weaken, and cohesive  
32 forces begin to dominate across the entire flow depth, but the cohesive matrix strength is still not  
33 high enough to support sand-sized particles. This balance between cohesive and turbulence forces  
34 further changes in the QLPFs, where, as concentration increases from  $C_0=12.1\%$ , an increasing  
35 amount of sand is incorporated in the fluid mud until a basal sand layer no longer forms at  
36  $C_0=16.5\%$ . The visual observation that sand grains fall at a slow rate through the fluid mud in low-  
37 concentration QLPFs, but are supported within the fluid mud in high-concentration QLPFs,  
38 suggests that the cohesive matrix becomes progressively stronger and eventually able to support  
39 the whole range of particle sizes.

40  
41  
42  
43  
44  
45  
46  
47  
48  
49 In the present experiments, the medium sand segregated from the kaolin clay at  $C_0\sim 11\%$ ,  
50 whilst the sand grains were fully mixed with the fluid mud at  $C_0>\sim 16\%$ . These threshold  
51 concentrations for the support of sand-sized particles are similar to the values of 11.3% and 14.3%  
52 reported by Sumner *et al.* (2009), who investigated the deposition of sand and clay from  
53 continuously decelerating suspension flows at various deceleration times and suspended sand  
54 concentrations. The present experimental data show that the threshold concentrations for partial  
55 particle segregation and full mixing depend on the grain size of the non-cohesive sediment, since  
56 the silt fraction mixed with kaolin clay to form a fluid mud at a lower suspended sediment  
57 concentration than the sand fraction ( $\sim 6\%$  versus  $\sim 11\%$ ). The phase boundaries between bed  
58  
59  
60

types I (full segregation and structured sand), II (full segregation and structureless sand), III (partial segregation) and IV (no segregation) of Sumner *et al.* (2009; their Fig. 1), which they used to distinguish between turbidites, hybrid beds and debrites, will therefore vary with the available sediment size fractions, as well as the concentration and type of clay, in the original suspension flow.

### 5.3 Bedform development phase

At the mean flow velocity of  $\sim 0.46 \text{ ms}^{-1}$  used in the present experiments, current ripples formed only in TFs, TETFs and LTPFs (i.e. at suspended sediment concentrations up to 8.0% by volume). Ripples started to develop within several minutes after the beginning of flow deceleration at  $C_o < 4\%$ , but at higher concentrations the first appearance of bedforms was delayed, with the time over which the initial flat bed remained stable increasing exponentially from 0.08 h at  $C_o = 5.1\%$  to 1.7 h at  $C_o = 8.0\%$ . The fluid-mud dominated beds below UTPFs and QLPFs remained stable for the full duration of the experiments. The present results show that the transition from ripples to a cohesive flat bed occurs over a remarkably narrow range of clay concentrations, since large ripples develop at  $C_o = 6.9\%$ , but not at  $C_o = 8.0\%$ . This cessation of bedform generation can be explained by an increase in bed shear strength, due to the greater amounts of cohesive clay incorporated into the bed, combined with a rapid decline in turbulence intensity across the phase boundary from LTPF to UTPF (Fig. 15d).

After the initial generation of bedforms, the current ripples rapidly increased in height and wavelength, reaching their equilibrium dimensions after approximately one hour at most sediment concentrations. Only near the upper clay concentration limit for bedform formation is it unclear if sufficient time was available to form equilibrium ripples. It is evident that equilibrium ripple height and wavelength increase at greater suspended sediment concentrations within TETFs and LTPFs. This trend is closely matched by near-bed  $RMS(u')$ , with high  $R^2$ -values of 0.95 and 0.96 for relationships between near-bed  $RMS(u')$  and ripple height and wavelength, respectively (Fig. 15). In view of previous work (Baas & Best, 2002, 2008; Baas *et al.* 2009), it is reasoned that the increased near-bed turbulence is caused by a change in flow dynamics inherent to transient turbulent flows, which is dominated by an internal shear layer (cf. Figs 2 and 3). However, another possibility is that the higher near-bed  $RMS(u')$  values result from higher production of turbulence over the bedforms, because larger ripples produce greater drag. The expected increase in drag coefficient from TF via TETF to LTPF can be estimated using Eqs 11 and 12 (Van Rijn, 1990, 1993):

$$C_d = 18 \log_{10} \left( \frac{12h}{k_s''} \right) \quad (11)$$

$$k_s'' = 20\gamma \frac{H_e^2}{L_e} \quad (12)$$

1 where  $C_d$  is the Chézy drag coefficient,  $h$  is flow depth,  $k_s''$  is the Nikuradze form roughness  
 2 height,  $\gamma$  is the ripple presence factor ( $\gamma=1$  in the present experiments), and  $H_e$  and  $L_e$  are  
 3 equilibrium ripple height and wavelength, respectively. Figure 17 illustrates that Eqs 11 and 12  
 4 produce a decrease in  $C_d$  (indicating increased drag) with increasing suspended sediment  
 5 concentration, but only of  $\sim 2\%$ , thus only making a minor contribution to the production of  
 6 turbulence. It can therefore be concluded that the bulk of the increase in  $RMS(u')$  values within TF,  
 7 TETF and LTPFs is caused by processes related to the presence of an internal shear layer, and  
 8 that this increase in  $RMS(u')$  causes the ripples to increase in their height and wavelength.  
 9 Visually, this contention is supported by the stronger separation zone vortex present in the troughs  
 10 of ripples formed within TETFs and LTPFs, which appears to enhance bed erosion and produces  
 11 unusually large backflow ripples (Fig. 16a). Although the increased turbulence intensity within the  
 12 ripple troughs could not be verified quantitatively in the present experiments, indirect support is  
 13 provided by the velocity time-series of transitional clay flows collected in the trough of a fixed ripple  
 14 profile by Baas & Best (2008). These fixed-ripple experiments showed that  $RMS(u')$  can increase  
 15 by a factor of two at the point of flow reattachment and by a factor of ten near the base of the  
 16 separation zone.  
 17

18 It is also worthwhile comparing the trends in near-bed  $RMS(u')$  from the present experiments  
 19 with those of the flat bed experiments at similar depth-averaged flow velocities reported by Baas *et al.*  
 20 (2009; their experimental series 3), since the phase boundary between LTPF and UTPF is at a  
 21 similar concentration ( $8.0\% < C_0 < 10.1\%$  for the rippled beds herein and  $8.9\% < C < 9.6\%$  for the flat  
 22 beds of Baas *et al.*, 2009). In the flat-bed experiments of Baas *et al.* (2009), near-bed  $RMS(u')$   
 23 increased from  $38 \text{ mm s}^{-1}$  to  $61 \text{ mm s}^{-1}$  from the TF to the LTPF-UTPF boundary, while the  
 24 equivalent increase for the rippled beds detailed herein is from  $66 \text{ mm s}^{-1}$  to  $91 \text{ mm s}^{-1}$ . This yields  
 25 an increase in  $RMS(u')$  of  $23 \text{ mm s}^{-1}$  and  $25 \text{ mm s}^{-1}$  for the flat and rippled bed, respectively, with  
 26 the insignificant difference of  $2 \text{ mm s}^{-1}$  between the two providing further support for the minor  
 27 contribution of increasing bed roughness to the enhancement of turbulence.  
 28

29 The bed sediment flux decreases as suspended sediment concentration increases at  
 30  $0\% < C_0 < 3.5\%$  and  $7\% < C_0 < 10\%$ , but the flux increases between  $C_0 \sim 3.5\%$  and  $C_0 \sim 7\%$  (i.e. in the  
 31 high-concentration TETF and LTPF; Fig. 15c). The decreasing bed sediment fluxes are likely  
 32 controlled by an increase in bed shear strength, and thus a decrease in sediment availability, as  
 33 progressively larger amounts of cohesive clay are incorporated into the bed. The range of clay  
 34 concentrations at which the bed sediment flux increases coincides with very high near-bed  
 35 turbulence intensities, and it is speculated that this produces higher bed shear stresses that  
 36 increase bed erosion, thus overcoming the high shear strength of the bed. However, since the bed  
 37 shear strength increases exponentially with clay concentration, this results in another reversal in  
 38 bed sediment flux at  $C_0 > 7\%$ . At these high clay concentrations, despite the fact that the LTPF has  
 39 the highest near-bed turbulence intensity of all the experimental flows, it appears that the bed was  
 40 stable enough to cause a dramatic decrease in the bed sediment flux (Fig. 15c). Figure 18  
 41  
 42  
 43  
 44  
 45  
 46  
 47  
 48  
 49  
 50  
 51  
 52  
 53  
 54  
 55  
 56  
 57  
 58  
 59  
 60

1  
2 summarises the competing forces of turbulence and cohesion in a conceptual model of bed shear  
3 strength and near-bed turbulent shear stress. This model assumes that ripples form only if the  
4 near-bed turbulent shear stress exceeds the yield strength of the sediment bed, which is  
5 expressed in Fig. 18 by the diagonal line of critical shear stress. Ripples can thus form only on the  
6 upper left-hand side of this line, with the bed sediment flux due to ripple migration increasing with  
7 increasing distance from this shear stress limit. At low yield strengths (e.g. Run 1), near-bed  
8 turbulent stresses dominate the bed sediment flux, but near-bed turbulence also works effectively  
9 against yield strength in high-concentration TETFs and LTPFs (e.g. Run 6), in spite of the higher  
10 bed shear strength. The dip in the bed sediment flux curve for low-concentration TETFs in Fig. 18  
11 represents conditions in which the increasing near-bed turbulent stress cannot keep pace with the  
12 increasing yield strength of the bed. The dramatic decrease in near-bed turbulence intensity in  
13 UTPFs and QLPFs (Runs 8-14), and the concurrent increase in yield strength, cause the bed  
14 sediment flux curve to rapidly cross the critical shear stress limit into the stable flat bed region of  
15 Fig. 18.

16  
17  
18  
19  
20  
21  
22  
23  
24  
25 The laboratory experiments described herein simulated rapidly waning-to-steady mixed-  
26 sediment flows, which showed reworking of the deposits formed in the early suspension settling  
27 phase through erosion and the generation of current ripple in the bedform development phase.  
28 This experimental procedure was different from the procedure used by Sumner *et al.* (2008, 2009),  
29 who formed deposits of sand and kaolin clay from suspension flows that decelerated linearly from  
30 very high velocity ( $\sim 3 \text{ m s}^{-1}$ ) to zero velocity. At the typical deceleration time of  $\sim 1$  minute applied  
31 herein, the experiments of Sumner *et al.* (2009) revealed: (i) clean, structureless sand overlain by a  
32 mud cap for TF and TETF (their deposit type II); (ii) thin structureless sand overlain by ungraded  
33 muddy sand and a mud cap for LTPF and UTPF (their deposit type III); and (iii) ungraded muddy  
34 sand with a mud cap for QLPF (their deposit type IV). In addition, Sumner *et al.* (2008, 2009) found  
35 that, for type II deposits formed from rapidly decelerated flows, sand segregated from the muddy  
36 suspension continuously during flow deceleration and this process continued after the flow had  
37 come to a halt. In the rapidly waning-to steady TF and TETF, bedform development commenced  
38 almost immediately after the sand and silt had settled from suspension. As these bedforms did not  
39 appear to climb upward, it is assumed that most, if not all, of the sand and silt had settled from  
40 suspension by the time the first current ripples formed on the bed. The deposits of the rapidly  
41 waning-to-steady TF and TETF had a bipartite granulometric texture, with sand overlain by silt (Fig.  
42 10), whereas the equivalent type II deposits of Sumner *et al.* (2008) displayed a normal grading  
43 without a clear grain-size break. This textural difference might be caused by the bimodal grain-size  
44 distribution of the non-cohesive sediment used in the present experiments (Fig. 5). It thus appears  
45 that the type II deposits of Sumner *et al.* (2009) will exhibit cross-stratification if a period of steady  
46 flow is present in the flow hydrograph. If such a period of steady flow is able to keep most of the  
47 cohesive sediment in suspension, the formation of a protective mud layer on top of the non-  
48 cohesive sediment layer will be inhibited, as was found in the type II deposits of Sumner *et al.*

1 (2009). This lack of protection subsequently permits reworking of the top of the deposit into current  
2 ripples. However, it should be straightforward to distinguish the type II deposits with reworked tops  
3 from the type I deposits (plane-parallel laminated and cross-laminated sand; Sumner *et al.*, 2008),  
4 since reworking will usually be restricted to the maximum depth of scour associated with the  
5 bedform troughs. The type III deposits of Sumner *et al.* (2009) contained a thick layer of ungraded  
6 muddy sand. Such a layer was absent from the deposits of rapidly waning-to-steady LTPF and  
7 UTPF, in which the fluid mud was deprived of sand. The high mobility of the fluid mud, combined  
8 with the consistently high levels of turbulence, for especially the LTPF, are inferred to have  
9 promoted the deposition through the fluid mud of any sand that remained in suspension after  
10 formation of the basal sand layer. Yet, this remaining suspended sand must have constituted small  
11 volumes, because the thickness of the basal sand layer in the LTPF and UTPF was similar to that  
12 of TF and TETF. Similar to the type II deposits, the type III deposits will exhibit cross-stratification if  
13 a period of steady flow is present. Sumner *et al.* (2009) interpreted their type IV deposits as the  
14 product of laminar flows that were strong enough to support all non-cohesive sediment. However, it  
15 appeared that at least some sand was able to settle onto the bed from the low-concentration  
16 rapidly waning-to-steady QLTFs. Again, this might be caused by rheological differences between  
17 the rapidly halted flows of Sumner *et al.* (2009) and the present experiments, where an initial rapid  
18 waning is followed by a period of steady flow.  
19  
20  
21  
22  
23  
24  
25  
26  
27  
28  
29  
30  
31  
32

## 33 **6. IMPLICATIONS FOR BEDFORMS, FACIES AND HYBRID BED FORMATION**

### 34 **6.1. General**

35  
36  
37  
38  
39 The central finding of this experimental study is that bedforms generated in turbulent flows and  
40 turbulence-modulated, cohesive flows differ greatly in their size, texture, sedimentary structure and  
41 migration rate. The unique properties of the current ripples and plane beds developing below  
42 rapidly-waned flows with transient turbulent behaviour documented herein could help to identify  
43 such flows and their depositional products, and to interpret key depositional processes, in modern  
44 and ancient sediments. Before exploring how these laboratory-based sedimentological data can be  
45 used for this purpose, it is important to emphasise that the number of physical variables controlling  
46 the dynamics of cohesive mixed sediment is larger than for non-cohesive sediment, and that the  
47 experiments herein cover only a subset of these variables. This significantly limits the extrapolation  
48 of the results to natural environments, in particular because the experiments comprised: (1) a  
49 single clay type, with specific rheological and cohesive properties; (2) a single flow velocity after  
50 flow deceleration, that was chosen to specifically position the flows within the current ripple regime;  
51 (3) a rapid rate of deceleration, which led to quick, en-masse deposition of the coarse, non-  
52 cohesive fraction, in particular at low suspended sediment concentrations; (4) a wide range of grain  
53 sizes in the non-cohesive fraction, which accentuated the sedimentary structures produced; (5) a  
54  
55  
56  
57  
58  
59  
60

constant initial volume of non-cohesive suspended sediment; and (6) relatively small total volumes of suspended sediment, resulting in deposits that were thin compared to most natural deposits. The need for additional mixed-sediment research is clear, but despite these limitations, several generic outcomes can be extracted from the experimental data.

## 6.2. Flow Reynolds number and bedform generation

Current ripples develop only in TFs, TETFs and LTPFs, because the turbulent shear stress is high and the bed shear strength is low when compared to UTPFs and QLPFs. In the present experiments, the upper limit of suspended sediment concentration for bedform development was 8%, but this concentration will depend on the flow shear velocity (cf. Baas *et al.*, 2009) as well as the exact composition and size of the sediment. Therefore, neither this concentration, nor any other single value, should be used as a general discriminator of bedform formation, as has been suggested previously for distinguishing turbidity currents from debris flows in deep-marine environments (e.g. Middleton, 1993; Shanmugam, 2000). A better dimensionless approach is to use the flow Reynolds number (Eq. 5), which Baas *et al.* (2009) have shown suitable for delineating the phase boundaries between turbulent, transitional and laminar clay flows. Herein, the Reynolds number at the clay concentration limit for bedform formation is between 8,300 and 19,500, which agrees well with  $Re=12,000\pm3,400$  for the LTPF-UTPF boundary in the flat-bed experiments of Baas *et al.* (2009). Thus, it can be concluded that the development of current ripples cannot take place in cohesive plug flows with a Reynolds number smaller than 12,000. Bedform development in flows with  $Re>12,000$  will occur only if the bed is formed by the flow itself, as in the present experiments, or if the bed shear stress is higher than the critical shear strength for sediment entrainment of beds that are formed independently. Although the flow Reynolds number approach is particularly useful for predicting mixed sediment facies when the flow properties are known, the reconstruction of flow properties from deposit properties, as needed in sedimentary geology, is more difficult, because it requires independent estimates of the physical parameters that constitute the Reynolds number.

## 6.3. Bedform dimensions and stratification in mixed mud-sand deposits

The equilibrium height and wavelength of the ripples in the TF correspond well with the equilibrium ripple dimensions for 0.095 mm sand quantified by Baas (1994) and those calculated from the current ripple predictors of Baas (1993):

$$H_e = 3.4 \log_{10}(D_{50}) + 18 \quad (13)$$

$$L_e = 75.4 \log_{10}(D_{50}) + 197$$

and Raudkivi (1997):

$$H_e = 18 D_{50}^{0.1} \quad (14)$$

$$L_e = 245 D_{50}^{0.35}$$

where  $D_{50}=0.084$  mm, and  $H_e$  and  $L_e$  are equilibrium ripple height and wavelength (in mm), respectively (Table 2). The current ripples in the transitional flows herein were up to 18.3 mm high and 203.0 mm long. Such large dimensions are uncommon for ripples in clean sand, as shown by the predicted height and wavelength of ripples at the upper grain-size limit of ripple formation ( $D_{50}=0.7$  mm: Table 2). Ripple height and wavelength might therefore be an appropriate sedimentological discriminator for turbulence-modulated flows, in particular if this is used in combination with other criteria. Transitional-current ripples consist of “dirty”, muddy sand, with the proportion of mud being higher in ripples formed under LTPFs than under TETFs. In the present experiments, the distribution of sand and mud within the ripples was a function of the stage of ripple development (Fig. 14): (1) thin, low-angle, cross-laminated sand that caps the muddy core of ripples is characteristic of early-stage development; (2) rhythmically-interbedded mud-sand cross-laminae represents intermediate-stage development; and (3) mixed mud-sand cross-lamination indicates late-stage development. The type of cross-lamination could therefore be a measure for the duration of bed reworking, and thus flow duration, but this can only be fully assessed when the processes of bedform development at a wider range of waning-to-steady transitional flow conditions have been established. The sequence of stratification types found in the present experiments will exist *only* if a flow forms a deposit with a distinct depositional grain-size break upon rapid deceleration (equivalent to the bipartite beds in the experiments) and if the grain-size break is at a shallower depth than the scour depth of the ripple troughs. Since the maximum scour depth of ripples is of the order of the bedform height, i.e. several tens of millimetres, these sedimentary structures will be confined to thin-bedded deposits (*sensu* McKee and Weir, 1953). Reworking of sediment across a grain-size break might extend to thick- and very-thick bedded bipartite deposits (*sensu* McKee and Weir, 1953) under transitional-flow conditions that allow the development of dunes, since the maximum scour depths of dunes can reach several hundreds of millimetres to several metres. In cases where the mobile bed exists before the clay concentration rises (as opposed to the decelerated flows herein that formed the initial bipartite bed), clays may become incorporated within the deposits. This has been illustrated by Simons *et al.* (1963), who documented clay lenses that were deposited in the ripple troughs, formed from current ripples migrating under bentonite-rich flows.

Other diagnostic criteria for recognising transitional flow deposits in outcrop and core could be more common, and are associated with the characteristically strong near-bed turbulence and cohesive nature of the mixed-sediment beds: (1) Deep erosional scours with steep, irregular edges appear typical of partly cohesive ripples in LTPFs; (2) This irregular topography is often infilled by non-cohesive sand, re-establishing a more triangular ripple shape (Fig. 16c); (3) Anomalously large, fine-grained, backflow ripples (typically 5 mm high) in the troughs of the larger ripples are

1  
2 preserved as an irregular layer of silt or mud below the foreset cross-laminae (Fig. 16a); and (4)  
3 Subvertical, pipe- or sheet-like fluidisation structures within the muddy fraction of the current  
4 ripples record the initially rapid deposition of sediment from suspension, followed by dewatering.  
5 This fluidisation may be caused by the pressure gradients associated with the strong turbulent  
6 velocity fluctuations over the ripple leeside, and possibly aided by loading of sand-silt upon the  
7 muddy layer beneath.  
8  
9  
10  
11

#### 12 13 **6.4. Ripple cross-lamination and massive turbiditic sandstones** 14 15

16  
17 In a theoretical study of the formation of massive turbiditic sandstones, Baas (2004) suggested  
18 that current ripples are ubiquitous below rapidly-decelerating turbidity currents, because these  
19 bedforms can form within several tens of seconds. Turbidites should therefore possess a division  
20 with ripple cross-lamination, unless there are special circumstances that prevent the formation of  
21 the ripples, or that destroy the ripples at a later stage. These speculations may apply not just to  
22 turbidites, but also to other deposits that are formed from rapidly-waned flows. The present  
23 experiments suggest an alternative mechanism for inhibiting bedform development. If a flow  
24 behaves as an UTPF or a QLPF after flow deceleration with  $Re < 12,000$ , insufficient turbulent  
25 shear stresses will exist in order to generate bedforms. Moreover, rapid deceleration of these flows  
26 may lead to the deposition of cohesive mud, with the high shear strength of these deposits then  
27 further inhibiting bedform development. The bipartite beds shown in Fig. 10 may thus be diagnostic  
28 products of UTPFs and QLPFs, although it should be remembered that variations to this  
29 sedimentary structure are possible depending on the grain-size distribution in the formative flow,  
30 and the degree of segregation of different grain sizes may thus be useful in distinguishing between  
31 UTPF and QLPF deposits.  
32  
33  
34  
35  
36  
37  
38  
39  
40  
41

#### 42 43 **6.5. Mixed mud-sand facies of decelerating flows** 44 45

46  
47 Although a more comprehensive understanding of the physical variables that control the  
48 dynamics of mixed cohesive sediments and their depositional products is required, the laboratory  
49 results presented herein can be used to propose preliminary models for the sedimentological  
50 properties of natural waning flows that comprise sand, silt and cohesive clay. For this purpose,  
51 several schematic sedimentary facies are presented (Fig. 19) that encapsulate variations in the  
52 structural and textural features of such deposits as a function of the initial suspended sediment  
53 concentration, rate of flow deceleration (based on the above comparison with the work of Sumner  
54 *et al.*, 2009), and the duration of post-deceleration steady flow.  
55  
56  
57  
58

59 Under conditions where the flow decelerates rapidly and the steady flow phase is very short or  
60 absent (i.e., equivalent to the continuously and rapidly decelerating flows of Sumner *et al.*, 2009),  
the sedimentary facies are expected to lack current lamination (Figs 19a-e), but they might show a



1 basal subfacies with inverse grading, caused by hindered settling (Bagnold, 1956) or kinetic  
2 sieving (Middleton, 1970; Legros, 2002) that is overlain by a subfacies with normal distribution  
3 grading, caused by differences in grain settling velocity. These textural features are typical of the  
4 facies associated with TF and TETF. The sediment size distribution in the formative flow  
5 determines if such facies exhibit grain-size breaks (as shown in Fig. 19a) or whether normal  
6 grading is more continuous (as in Sumner *et al.*, 2009). In the LTPF and UTPF facies, the finer  
7 non-cohesive fraction will be mixed with the cohesive clay fraction to form a mud deposit on top of  
8 the basal sand (Figs 19b-c). Evidence for soft sediment deformation within this mud might point to  
9 its fluid-mud origin. The basal sand should be relatively thin in the sedimentary facies of mixed-  
10 sediment QLPFs (Fig. 19d), or absent altogether (Fig. 19e), as at least part of the sand is  
11 incorporated into the cohesive mud. In addition to the presence or absence of the basal sand in the  
12 QLPF facies, the clay concentration in the formative flow can also be estimated qualitatively using  
13 the vertical distribution of sand in the muddy subfacies, with lower concentration QLPFs producing  
14 deposits in which sand tends to accumulate near the base of the mud (Fig. 19d) and higher  
15 concentration QLPF deposits exhibiting a more homogeneous distribution of sand grains in the  
16 vertical (Fig. 19e).

17  
18  
19  
20  
21  
22  
23  
24  
25  
26  
27  
28 The inferred sedimentary facies of the rapidly decelerated to steady UTPF and QLPF, shown in  
29 Figs 19c-e, are similar to the deposit types III and IV of Sumner *et al.* (2009), which were formed  
30 from linearly decelerated flows with a comparable rheology to the present experiments. Sumner *et al.*  
31 (2009) demonstrated that these deposit types form at a wide range of flow deceleration rates. It  
32 may thus be difficult to estimate the rates of deceleration, or the presence or absence of steady  
33 flow phases, from UTPF and QLPF deposits, based solely on their textural properties. In contrast,  
34 the rate of flow deceleration and the duration of post-deceleration steady flow could well be  
35 reflected in the sedimentary facies of TF, TETF and LTPF. Rapid flow deceleration without a  
36 prolonged period of steady flow will produce structureless facies, as described above, but if flow  
37 deceleration is more gradual or if a period of steady flow follows the phase of rapid flow  
38 deceleration, the TF, TETF and LTPF facies should be stratified (Figs 19f-n). The available  
39 laboratory data suggest that the type of stratification depends on the duration of the steady flow  
40 phase (Figs 19f-m), and that the stratification will also be different for flows that decelerate  
41 continuously at a slow rate (Fig. 19n; Sumner *et al.*, 2009). Steady TFs, TETFs and LTPFs may  
42 also be able to rework the original deposit into bedforms that grow in height and length with time by  
43 scouring progressively deeper into the underlying structureless facies, thus forming the temporal  
44 sequence of sedimentary structures depicted in Figs 14 and 16. The corresponding sedimentary  
45 facies (Fig. 19f-m) could thus provide a relative measure for the duration of the steady flow phase.  
46 For example, a tripartite bed comprising, from base to top, structureless sand, deformed mud, and  
47 low-angle cross stratified sand (Fig. 19i) might signify a steady LTPF of shorter duration than a  
48 bipartite bed comprising high-angle cross-stratified sandy mud overlying structureless sand (Fig.  
49 19m). This method for estimating flow duration should however be treated with caution, because  
50  
51  
52  
53  
54  
55  
56  
57  
58  
59  
60

1  
2 the rate of bedform development is also likely to be dependent on flow velocity (cf. Baas, 1994,  
3 1999), although this dependency has not yet been investigated for mixed sand-mud systems.  
4  
5

## 6.6. Processes controlling the facies of decelerating flows

6  
7  
8  
9

10 In sedimentary facies produced by slow, continuous deceleration of TF, TETF and possibly  
11 LTPF, Sumner *et al.* (2008, 2009) found that the formation of current lamination takes place  
12 simultaneously with sediment deposition. Such facies show evidence of *depositional* sedimentary  
13 structures in waning flow, such as Bouma-type sequences (Bouma, 1962), climbing ripples,  
14 aggradational upper-stage plane bed laminae, and normal grading (Fig. 19). This is in contrast to  
15 the sedimentary facies produced by the rapidly decelerated to steady TF, TETF and LTPF,  
16 investigated herein, which should exhibit *erosional* sedimentary structures, such as internal  
17 erosional scours and retention of the reworked sediment within the bedform foreset laminae. This  
18 evidence for erosion and reworking is expected to occur more frequently near the top of the facies,  
19 thus preserving at least some of the original structureless sediment underneath.  
20  
21  
22  
23  
24  
25

26 All deposits of the experimental TFs, TETFs, LTPFs and UTPFs contain remarkably clean basal  
27 sand, suggesting that grain-size segregation directly after flow deceleration is essential for the  
28 generation of these deposits. The capacity of these flows to carry non-cohesive sediment is  
29 governed mainly by the grain settling velocity (approximated by grain size for the sake of  
30 convenience), the magnitude of upward-directed turbulence and the cohesive matrix strength. The  
31 turbulence support of sand grains is considered to be of minor importance for the experimental  
32 flows investigated herein, because sand quickly settled onto the bed even in the LTPFs, where  
33 RMS( $u'$ ) reached peak values. Full cohesive support of sand grains was found only at suspended  
34 sediment concentrations well within the QLPF regime. Silt-sized sediment, however, segregated  
35 from the clay suspension only in TF and TETF, but mixed with the suspended clay, and formed  
36 fluid mud layers, in the LTPF, UTPF and QLPF facies. Hence, silt grains are supported at lower  
37 levels of turbulence and at lower cohesive matrix strength than sand grains, owing to their lower  
38 settling velocity. These differences in sediment-carrying capacity, and the effect on sedimentary  
39 facies, are depicted graphically in Fig. 20, in which the total grain support is assumed to be equal  
40 to the sum of the grain support by upward-directed turbulence and flow cohesion. This approach  
41 should be regarded as a first-order approximation, because it ignores the feedback relationships  
42 between turbulence and cohesive forces discussed in the introduction. Following Eqs 6 and 7,  
43 cohesive support increases exponentially with increasing clay concentration, whilst turbulence  
44 support reaches a maximum in LTPF (thin lines in Fig. 20). The total support thus increases at  
45 greater clay concentrations in TF, TETF and LTPF, but this trend is interrupted by a decrease in  
46 total support for UTPF (thick line in Fig. 20), due to the dramatic decrease in turbulent grain  
47 support (cf. Fig. 15) that is inferred to outbalance the increased cohesive support within UTPF.  
48 Figure 20 also shows schematically the carrying capacity thresholds for sand and silt, which were  
49  
50  
51  
52  
53  
54  
55  
56  
57  
58  
59  
60

1  
2 reconstructed using the evidence for size segregation and mixing in the laboratory-derived  
3 sedimentary facies. In summary, for the specific experimental conditions considered herein: (a) TF  
4 and TETF do not carry any sand or silt, and these size classes are well separated in the  
5 corresponding facies; (b) LTPF and UTPF carry silt, but not sand, resulting in a mixed silt-clay  
6 (mud) overlying a basal sand in the matching facies; and (c) QLPF carries both sand and silt, with  
7 the corresponding facies being dominated by sandy mud. However, it is likely that these facies will  
8 vary for different flows and suspended sediments, and it is even possible that facies type  
9 boundaries will be crossed. Speculation on the decrease in total carrying capacity of UTPFs (Fig.  
10 20) is particularly fascinating. In these flows, if the flow velocity or sediment concentration is  
11 decreased, but the flow remains within the UTPF regime, then the total grain carrying capacity may  
12 decrease further than in the present experiments, provoking a change from the bipartite facies  
13 shown in Fig. 20 to a facies in which the sand, silt and clay are fully separated, thus resembling the  
14 TF and TETF facies. This would defy the common assumption that grain support increases as  
15 suspended sediment concentration increases in high-density clay-laden flows, and complicate  
16 process reconstructions in the rock record. On the other hand, it could explain the frequent  
17 occurrence of basal sands in natural sedimentary facies that are associated with high-  
18 concentration sediment gravity flows, such as debrites, high-density turbidity current deposits, and  
19 hybrid deposits (*sensu* Haughton *et al.*, 2009).  
20  
21  
22  
23  
24  
25  
26  
27  
28  
29  
30  
31  
32

### 33 **6.7. A revised model for hybrid bed formation**

34  
35  
36 Based on outcrop and core data from a large number of deep-marine sedimentary successions,  
37 Haughton *et al.* (2009) proposed an idealised hybrid sediment gravity flow deposit, comprising,  
38 from bottom to top (Fig. 21): (a) an H1 division: clean, graded to ungraded, structureless,  
39 dewatered sand with a sharp planar base and a top that may be sharp with sand injections or  
40 gradational with banding (*sensu* Lowe & Guy, 2000); (b) an H2 division: alternating bands of mud-  
41 poor sand and mud-rich sand; (c) an H3 division: muddy sand with mud clasts, sand patches, sand  
42 injections, outsized granules and shear fabrics; (d) an H4 division: thin, plane parallel laminated  
43 and ripple cross-laminated sand; (e) an H5 division: pseudonodular and/or massive mud.  
44 According to Haughton *et al.* (2009), hybrid sediment gravity flow deposits are “emplaced by a  
45 combination of fluidal and plastic flow recording switching between turbulent, transitional and  
46 laminar behaviour”, following longitudinal flow transformations as sediment gravity flows travel  
47 basinward. In the model of Haughton *et al.* (2009), the H1 division is the depositional product of a  
48 forerunner turbidity current, the H2 division is formed by a flow with alternating laminar and  
49 turbulent behaviour, the H3 division represents a trailing debris flow, and the H4 and H5 divisions  
50 are equivalent to Bouma  $T_{bc}$  and  $T_e$  divisions, thus originating from a low-density turbidity current in  
51 the tail of the hybrid event (Fig. 21). Talling *et al.* (2010) described deposits from the outer  
52 Mississippi Fan that also comprise a basal clean sand overlain by a debritic mud, but favoured the  
53  
54  
55  
56  
57  
58  
59  
60

1  
2 model of Sumner *et al.* (2009) for vertical size segregation in cohesive flows over Haughton *et al.*  
3 (2009)'s model of longitudinal flow transformation to explain the origin of these beds. The basal  
4 clean sand layer was found to terminate at the same location as the overlying debrite, which led  
5 Talling *et al.* (2010) to conclude that these divisions were formed by the same flow, i.e. a debris  
6 flow with relatively low cohesive matrix strength from which sand particles were able to settle onto  
7 the bed (equivalent to deposit type III of Sumner *et al.*, 2009). This genetic model closely matches  
8 the formation of the LTPF, UTPF facies in the present laboratory study. The hybrid flow model of  
9 Haughton *et al.* (2009) is well documented, but it does not leave much room for vertical  
10 segregation of non-cohesive and cohesive size fractions in a single flow type (cf. Figs 19 and 20).  
11 It is hypothesised herein that this vertical segregation may take place in conjunction with  
12 longitudinal transformation into different turbulent, transitional and laminar flow components (Fig.  
13 21). The structureless H1 division may not be necessarily linked to a forerunner high-density  
14 turbidity current (Haughton *et al.*, 2009). A sediment gravity flow that behaves as a rapidly or more  
15 gradually decelerating LTPF, UTPF or low-concentration QLPF, and hence with a pronounced plug  
16 region instead of pervasive turbulence, will produce a basal sand with textural properties that is  
17 similar to the H1 division. These properties include a flat, sharp base, a general lack of internal  
18 stratification and a clean texture. The occasional presence of current lamination near the top of H1  
19 divisions and other basal sands (e.g., Talling *et al.*, 2004, 2010) could denote reworking of the  
20 sand during a phase of steady flow. Moreover, the banding in the H2 division of hybrid event beds  
21 could signify mixing and reworking of cohesive and non-cohesive sediment at the interface of the  
22 basal sand and an overlying mobile, possibly sandy, fluid mud in the same flow that formed the  
23 basal sand, thus without the need to invoke separate flow components and complex longitudinal  
24 fluctuations. The unique character of the H3 division (e.g., large mud clasts, oversized granules and  
25 exotic material), as well as the H4 and H5 divisions, precludes a direct relationship with the H1 and  
26 H2 divisions. These divisions are therefore most likely to be the product of longitudinal flow  
27 transformation (Haughton *et al.*, 2009). However, if the basal structureless sand and the banded  
28 subfacies were formed by LTPF or UTPF there may not be such a dramatic longitudinal transition  
29 in flow rheology as in the hybrid event model Haughton *et al.* (2009).  
30  
31  
32  
33  
34  
35  
36  
37  
38  
39  
40  
41  
42  
43  
44  
45  
46  
47  
48  
49

## 50 51 **7. CONCLUSIONS**

52  
53  
54 Flows that contain suspended sediment are ubiquitous within all sedimentary environments and  
55 yet there is currently a limited understanding of the influence of high sediment concentrations on  
56 the formation of bedforms and their resultant sedimentary structures. Past work has illustrated the  
57 unique properties of open-channel flows with transient turbulent behaviour that are present under a  
58 wide range of conditions between turbulent flows and those that adopt quasi-laminar flow  
59 properties. Additionally, rapidly-decelerated flows of high sediment concentration are not limited to  
60

1  
2 open-channel flow, and they are likely to occur in many sedimentary environments, for example as  
3 a response to flood waning or flow deceleration as bed slope decreases. The present study has  
4 sought to investigate the nature of bedform development and deposition under decelerated  
5 sediment-laden flows of different clay concentration. Although idealised in their coverage of key  
6 variables, these experiments highlight the significant role played by fine sediment concentration in  
7 affecting bedform generation, and show that the recognition of deposits formed by these flows in  
8 the sedimentary record may be helped by such experimental studies. Ten conclusions can be  
9 drawn:

- 10 1. The different flow phases defined in past work over smooth walls and fixed bedforms can also  
11 be identified over mobile beds with bedform roughness. As clay concentration increases, these  
12 flow phases proceed from turbulent flow (TF) to turbulence-enhanced transitional flow (TETF),  
13 lower transitional plug flow (LTPF), upper transitional plug flow (UTPF) and finally quasi-  
14 laminar plug flow (QLPF).
- 15 2. Rapid initial sedimentation always forms planar beds, with the nature of these beds a function  
16 of the nature of the flow phase. These facies are similar to those presented by Sumner *et al.*  
17 (2009), although it is shown herein that their phase boundaries will vary as a function of  
18 sediment size fractions, as well as clay concentration and clay type. These initial planar beds  
19 may be reworked into rippled beds, if a period of steady flow is present. With increasing  
20 suspended clay concentration, ripples first increase in height and wavelength under TETF and  
21 LTPF regimes, which is attributed to the additional turbulence generated under these flows that  
22 cause greater leeside erosion.
- 23 3. As clay concentration increases further from LTPF, ripples quickly cease to exist under the  
24 UTPF and QLPF conditions investigated herein. This appears due to turbulence suppression  
25 as the nature of the flow changes, as well as due to the increasing shear strength of the bed  
26 sediment that becomes more difficult to erode as clay concentration increases.
- 27 4. With increasing suspended sediment concentration, the flux of bedload sediment first  
28 decreases, due to increased bed shear strength, and then increases, due to enhanced near-  
29 bed turbulence and subsequent increased erosion rate, but eventually falls rapidly as both  
30 turbulence suppression and the shear strength of the bed increase.
- 31 5. The stratification within ripples formed under rapidly-decelerated to steady transitional flows  
32 reflects the availability of sediment from a bipartite bed that initially consists of settled medium  
33 sand and then fine sediment. The exact nature of the ripple cross-stratification in these flows is  
34 a direct function of the duration of the formative flow.
- 35 6. Current ripples cannot form in cohesive plug flows with a flow Reynolds number smaller than  
36 12,000, and in this case beds lacking any cross-lamination are likely to form on flow  
37 deceleration.

- 1  
2 7. No single sediment concentration can be used to discriminate different types of bedform  
3 formation in transitional flows, because the development of bedforms is also governed by the  
4 flow shear velocity and the physical properties of the suspended and bed sediment.  
5  
6
- 7 8. A new facies model for decelerated cohesive (sand-mud) sediment flows is outlined that  
8 accounts for suspended clay concentration, initial rate of deceleration, and the duration of any  
9 post-deceleration steady flow.  
10
- 11 9. A conceptual model of sediment segregation and mixing for mixed cohesive sediment flows is  
12 proposed. This model suggests that there may not always be a continuous increase in grain  
13 support within the flow as clay concentration increases. Such variation in grain support with  
14 sediment concentration may be a key mechanism that enables clean sands to be deposited at  
15 the base of high-concentration mud-rich gravity flows.  
16  
17
- 18 10. A new model for hybrid beds is proposed that explains the previously documented structural  
19 and textural features (*sensu* Haughton *et al.*, 2009) in terms of a combination of vertical  
20 segregation and longitudinal flow transformation.  
21  
22  
23  
24  
25

26 The present study has presented the first fully quantitative data on mobile bed sedimentation, and  
27 the first experimental data on bedform stratification, formed by decelerated sediment-laden flows,  
28 but under a restricted range of flow conditions. Further work is urgently required to expand the  
29 range of flow boundary conditions, and hence deposits and bedforms studied, to include dune-  
30 scale bedforms, as well as how these bedforms are represented within the ancient sedimentary  
31 record. The preliminary facies models, and the conceptual model of segregation and mixing,  
32 presented herein should assist in extrapolating the experimental data to natural processes and  
33 products.  
34  
35  
36  
37  
38  
39  
40  
41

## 42 **8. ACKNOWLEDGEMENTS**

43  
44  
45 We are very grateful to the UK Natural Environment Research Council for grant NE/C514823/1 that  
46 enabled this research to be undertaken at the Sorby Environmental Fluid Dynamics Laboratory,  
47 whilst JHB and JLB were at Leeds. Gareth Keevil is thanked for his support in the laboratory. We  
48 also acknowledge the thorough and highly stimulating comments on an earlier version of this paper  
49 by Esther Sumner, Joris Eggenhuisen, Associate Editor Peter Talling, Journal Editor Stephen Rice,  
50 and an anonymous reviewer.  
51  
52  
53  
54  
55  
56  
57  
58

## 59 **9. REFERENCES**

60

1  
2 **Amy, L.A. and Talling, P.J.** (2006) Anatomy of turbidites and linked debrites based on long  
3 distance (120X30 km) bed correlation, Marnoso Arenacea Formation, northern Apennines, Italy.  
4 *Sedimentology*, **53**, 161-212.

5  
6  
7 **Amy, L.A., Talling, P.J., Peakall, J., Wynn, R.B., and Arzola Thynne, R.G.** (2005) Bed  
8 geometry used to test recognition criteria of turbidites and (sandy) debrites. *Sedimentary Geology*,  
9 **179**, 163-174.

10  
11 **Arnott, R.W.C. and Hand, B.M.** (1989) Bedforms, primary structures and grain fabric in the  
12 presence of suspended sediment rain. *Journal of Sedimentary Petrology*, **59**, 1062-1069.

13  
14 **Ashley, G.M.** (1990) Classification of large-scale subaqueous bedforms: a new look at an old  
15 problem. *Journal of Sedimentary Petrology*, **60**, 160-172.

16  
17  
18 **Baas, J.H.** (1993) Dimensional analysis of current ripples in recent and ancient depositional  
19 environments. *Geologica Ultraiectina*, **106**, 199 pp.

20  
21 **Baas, J.H.** (1994) A flume study on the development and equilibrium morphology of small-scale  
22 bedforms in very fine sand. *Sedimentology*, **41**, 185-209.

23  
24 **Baas, J.H.** (1999) An empirical model for the development and equilibrium morphology of current  
25 ripples in fine sand. *Sedimentology*, **46**, 123-138.

26  
27  
28 **Baas, J.H.** (2004) Conditions for formation of massive turbiditic sandstones by primary  
29 sedimentary processes. *Sedimentary Geology*, **166**, 293-310.

30  
31 **Baas, J.H. and Best, J.L.** (2002) Turbulence modulation in clay-rich sediment-laden flows and  
32 some implications for sediment deposition. *Journal of Sedimentary Research*, **72**, 336-340.

33  
34 **Baas, J.H. and Best, J.L.** (2008) The dynamics of turbulent, transitional and laminar clay-laden  
35 flow over a fixed current ripple. *Sedimentology*, **55**, 635-666.

36  
37  
38 **Baas, J.H. and Best, J.L.** (2009) On the flow of natural clay suspensions over smooth and rough  
39 beds. *ERCOFTAC Bulletin*, **78**, 58-63.

40  
41 **Baas, J.H., Best, J.L., Peakall, J. and Wang, M.** (2009) A phase diagram for turbulent,  
42 transitional, and laminar clay suspension flows. *Journal of Sedimentary Research*, **79**, 162-183.

43  
44 **Bagnold, R.A.** (1954) Experiments on a gravity-free dispersion of large, solid spheres in a  
45 Newtonian fluid model shear. *Royal Society of London, Proceedings*, **A225**, 49-63.

46  
47 **Bagnold, R.A.** (1956) The flow of cohesionless grains in fluids. *Royal Society of London,*  
48 *Philosophical Transactions*, **A249**, 235-297.

49  
50  
51 **Best, J.L.** (1992) Sedimentology and event timing of a catastrophic volcanoclastic mass flow,  
52 Volcan Hudson, Southern Chile. *Bulletin of Volcanology*, **54**, 299-318.

53  
54 **Best, J.L., Kirkbride, A.D. and Peakall, J.** (2001) Mean flow and turbulence structure of  
55 sediment-laden gravity currents: new insights using ultrasonic Doppler velocity profiling. In:  
56 *Particulate Gravity Currents* (Eds W.D. McCaffrey, B.C. Kneller and J. Peakall), *IAS Special*  
57 *Publications*, **31**, 159–172.

58  
59  
60 **Bouma, A.H.** (1962) *Sedimentology of Some Flysch Deposits: a Graphic Approach to Facies*  
*Interpretation*. Elsevier, Amsterdam, 168 pp.

- 1  
2 **Coles, D.** (1956) The law of the wake in the turbulent boundary layer. *Journal of Fluid Mechanics*,  
3 **1**, 191-226.
- 4  
5 **Dasgupta, P.** (2003) Sediment gravity flow - the conceptual problems. *Earth-Science Reviews*,  
6 **62**, 265-281.
- 7  
8 **Haughton, P., Davis, C., McCaffrey, W. and Barker, S.** (2009) Hybrid sediment gravity flow  
9 deposits - Classification, origin and significance. *Marine and Petroleum Geology*, **26**, 1900-1918.
- 10  
11 **Legros, F.** (2002) Can dispersive pressure cause inverse grading in grain flows? *Journal of*  
12 *Sedimentary Research*, **72**, 166-170.
- 13  
14  
15 **Liu, K.F. and Mei, C.C.** (1990) Approximate equations for the slow spreading of a thin sheet of  
16 Bingham plastic fluid, *Physics of Fluids*, **A2**, 30-36.
- 17  
18 **Lowe, D.R. and Guy, M.** (2000) Slurry-flow deposits in the Britannia Formation (Lower  
19 Cretaceous), North Sea: a new perspective on the turbidity current and debris flow problem.  
20 *Sedimentology*, **47**, 31-70.
- 21  
22  
23 **McKee, E.D. and Weir, G.W.** (1953) Terminology for stratification and cross-stratification in  
24 sedimentary rocks. *Geological Society of America Bulletin*, **64**, 381-389.
- 25  
26 **Middleton, G.V.** (1967) Experiments on density and turbidity currents. III. Deposition of sediment.  
27 *Canadian Journal of Earth Sciences*, **4**, 475-505.
- 28  
29 **Middleton, G.V.** (1970) Experimental studies related to problems of flysch sedimentation. In:  
30 Flysch Sedimentology in North America (Ed. J. Lajoie), *Geological Association of Canada, Special*  
31 *Paper*, **7**, 253-272.
- 32  
33  
34 **Middleton, G.V.** (1993) Sediment deposition from turbidity currents. *Annual Review of Earth*  
35 *Sciences*, **21**, 89-114.
- 36  
37 **Mitchener, H. and Torfs, H.** (1996) Erosion of mud/sand mixtures. *Coastal Engineering*, **29**, 1-  
38 25.
- 39  
40  
41 **Mulder, T. and Alexander, J.** (2001) The physical character of subaqueous sedimentary density  
42 flows and their deposits. *Sedimentology*, **48**, 269-299.
- 43  
44 **Mulder, T. and Cochonat, P.** (1996) Classification of offshore mass movements. *Journal of*  
45 *Sedimentary Research*, **66**, 43-57.
- 46  
47 **Packman, A. I. and MacKay, J. S.** (2003) Interplay of stream-subsurface exchange, clay particle  
48 deposition, and streambed evolution, *Water Resources Research*, **39**, 1097-1105.
- 49  
50  
51 **Pierson, T.C. and Scott, K.M.** (1985) Downstream dilution of a lahar: Transition from debris flow  
52 to hyperconcentrated streamflow. *Water Resources Research*, **21**, 1511-1524.
- 53  
54 **Raudkivi, A.J.** (1997) Ripples on stream bed. *Journal of hydraulic Engineering*, **123**, 58-64.
- 55  
56 **Shanmugam, G.** (2000) 50 years of the turbidite paradigm (1950s-1990s): deep-water processes  
57 and facies models - a critical perspective. *Marine and Petroleum Geology*, **17**, 285-342.
- 58  
59 **Simons, D.B., Richardson, E.V. and Haushild, W.L.** (1963) *Some effects of fine sediment on*  
60 *flow phenomena*. US Geol Survey Water Supply Paper 1498-G, 45pp.



1  
2 **Stow, D.A.V. and Johansson, M.** (2000) Deep-water massive sands: nature, origin and  
3 hydrocarbon implications. *Marine and Petroleum Geology*, **17**, 145-174.

4  
5 **Sumner, E.J., Amy, L.A. and Talling, P.J.** (2008) Deposit structure and processes of sand  
6 deposition from decelerating sediment suspensions. *Journal of Sedimentary Research*, **78**, 529-  
7 547.

8  
9  
10 **Sumner, E.J., Talling, P.J. and Amy, L.A.** (2009) Deposits of flows transitional between turbidity  
11 current and debris flow. *Geology*, **37**, 991-994.

12  
13 **Takeda, Y.** (1991) Development of an ultrasound velocity profile monitor. *Nuclear Engineering*  
14 *and Design*, **126**, 277-284.

15  
16 **Talling, P.J., Amy, L.A., Wynn, R.B., Peakall, J. and Robinson, M.** (2004) Beds comprising  
17 debrite sandwiched within co-genetic turbidite: origin and widespread occurrence in distal  
18 depositional environments. *Sedimentology*, **51**, 163-194.

19  
20  
21 **Talling, P.J., Wynn, R.B., Schmidt, D.N., Rixon, R., Sumner, E. and Amy, L.** (2010) How did  
22 thin submarine debris flows carry boulder-sized intraclasts for remarkable distances across low  
23 gradients to the far reaches of the Mississippi Fan? *Journal of Sedimentary Research*, **80**, 829-  
24 851.

25  
26  
27 **Traykovski, P., Geyer, W.R., Irish, J.D. and Lynch, J.F.** (2000) The role of wave-induced  
28 density-driven fluid mud flows for cross-shelf transport on the Eel River continental shelf.  
29 *Continental Shelf Research*, **20**, 2113-2140.

30  
31  
32 **Van Den Berg, J.H.** (1987) Bedform migration and bed-load transport in some rivers and tidal  
33 environments. *Sedimentology*, **34**, 681-698.

34  
35  
36 **Van Maren, D.S., Winterwerp, J.C., Wang, Z.Y. and Pu, Q.** (2009) Suspended sediment  
37 dynamics and morphodynamics in the Yellow River, China. *Sedimentology*, **56**, 785-806.

38  
39  
40 **Van Rijn, L.C.** (1990) *Principles of Fluid Flow and Surface Waves in Rivers, Estuaries, Seas and*  
41 *Oceans*. Aqua Publications, Amsterdam, 335 pp.

42  
43 **Van Rijn, L.C.** (1993) *Principles of Sediment Transport in Rivers, Estuaries and Coastal Seas*.  
44 Aqua Publications, Amsterdam, 700 pp.

45  
46 **Wan, Z.** (1982) *Bed material movement in hyperconcentrated flow*. Institute of Hydrodynamics  
47 and Hydraulic Engineering, Lyngby, Technical University of Denmark, Series Paper, pp. 16-24.

48  
49 **Wang, X., Wang, Z.Y., Yu, M., and Li, D.** (2001) Velocity profile of sediment suspensions and  
50 comparison of log-law and wake-law. *Journal of Hydraulic Research*, **39**, 211-217.

51  
52  
53 **Wang, Z. and Plate, E.J.** (1996) A preliminary study on the turbulence structure of flows on non-  
54 Newtonian fluid. *Journal of Hydraulic Research*, **34**, 345-361.

1  
2  
3  
4  
5  
6  
7  
8  
9  
10  
11  
12  
13  
14  
15  
16  
17  
18  
19  
20  
21  
22  
23  
24  
25  
26  
27  
28  
29  
30  
31  
32  
33  
34  
35  
36  
37  
38  
39  
40  
41  
42  
43  
44  
45  
46  
47  
48  
49  
50  
51  
52  
53  
54  
55  
56  
57  
58  
59  
60

## FIGURE CAPTIONS

**Table 1** – Experimental parameters.

**Table 2** – Comparison of equilibrium ripple dimensions.

**Figure 1** – Clay flow phase diagram of Baas *et al.* (2009). The coloured symbols denote flows investigated in the present paper.

**Figure 2** – Schematic models of turbulent, transitional and quasi-laminar clay flows over a smooth, flat bed. The graphs to the left of the models denote characteristic velocity time series at various heights in the flows. The graphs to the right of the models represent characteristic vertical profiles of dimensionless downstream velocity ( $\bar{U} / \bar{U}_{\max}$ ) and root-mean-square of downstream velocity ( $RMS(u')$ ). Modified after Baas *et al.* (2009).

**Figure 3** - Conceptual models showing the changing dynamics of flow in the leeside of a fixed, flow-transverse bedform, as a function of increasing clay concentration. Modified after Baas & Best (2008).

**Figure 4** – Schematic diagram of the experimental set-up. UDVP = Ultrasonic Doppler Velocity Profilers.

**Figure 5** – Grain-size distribution curves of the cohesive and non-cohesive fractions used in the experiments. The frequencies for both fractions add up to 100%. The size class width is  $1/6\phi$ . The non-cohesive fraction was prepared by mixing two types of spherical glass beads ( $D_{50}=0.044$  mm and  $D_{50}=0.084$  mm) with two types of natural medium sand ( $D_{50}=0.283$  mm and  $D_{50}=0.310$  mm) in order to produce a sediment with a wide range of grain sizes.

**Figure 6** – Initial clay concentration plotted against  $\beta$  that is used in Eq. 10. The dashed lines indicate one standard deviation around the mean.

**Figure 7** – Vertical profiles of time-averaged downstream flow velocity (top) and the root-mean-square of downstream velocity (bottom) for selected experimental runs.

**Figure 8** - Vertical profiles of the root-mean-square of downstream velocity for lower transitional plug flows. Note that  $RMS(u')$ -values change with time.

1  
2  
3  
4  
5  
6  
7  
8  
9  
10  
11  
12  
13  
14  
15  
16  
17  
18  
19  
20  
21  
22  
23  
24  
25  
26  
27  
28  
29  
30  
31  
32  
33  
34  
35  
36  
37  
38  
39  
40  
41  
42  
43  
44  
45  
46  
47  
48  
49  
50  
51  
52  
53  
54  
55  
56  
57  
58  
59  
60

**Figure 9** – Time series of downstream velocity at ~6 mm above the bed in Run 7 ( $C_0=8.0\%$ ) at 3 different points in time. Note the pronounced saw-tooth shaped velocity fluctuations at  $t=0.17$  h, and to a lesser degree at  $t=1$  h.

**Figure 10** – Thickness and textural features of deposits formed after rapid flow deceleration and just before bedform development commenced. The question mark denotes estimated thickness, because of difficulties in recognising the flow-bed interface. Scale on photograph is in inches (top) and centimetres (bottom). The information above the graph refers to the boundary concentration for bedform development that occurred after the formation of the initial flat bed.

**Figure 11** – Temporal development of fluid mud layer thickness in the upper transitional plug flow and the quasi-laminar plug flows.

**Figure 12** – Sidewall photographs of final bedforms in selected experimental runs. Note the increase in ripple height and wavelength with increasing suspended sediment concentration and the muddy character of the ripple cores in Run 7 ( $C_0=8.0\%$ , shown by light colours).

**Figure 13** – Bedform height and wavelength development curves for selected runs in one turbulent flow and three lower transitional plug flows. Dashed lines indicate one standard deviation around the mean.

**Figure 14** – Photographs and schematic drawings of bedforms in progressive stages of development starting from an initial flat bed. The drawings are valid for TF, TETF and LTPF. The photographs are from Run 6 ( $C_0=6.9\%$ ), in which the fine-grained top of the initial flat bed (at  $t=0.26$  h) was more cohesive than in runs with lower suspended clay concentrations. Scale on photographs is in inches (top) and centimetres (bottom).

**Figure 15** - Relationships between initial suspended sediment concentration and (a) equilibrium bedform height, (b) equilibrium bedform wavelength, (c) bed sediment flux and (d)  $RMS(u')$ .

**Figure 16** – (a) Schematic drawing of a current ripple with prominent backflow ripples in Run 6 ( $C_0=6.9\%$ ). This ripple corresponds to the bedform at  $t_4$  in Fig. 14. Not to scale. (b) Photograph and labelled drawing of characteristic bedforms in Run 7 ( $C_0=8.0\%$ ) at  $t=1.08$  h. (c) Photograph and labelled drawing of characteristic bedforms in Run 7 at  $t=1.5$  h. Note that the core of firm mud in (b) and (c) affects bedform properties. See text for details.

**Figure 17** – Relationship between initial suspended sediment concentration and Chézy coefficient calculated for the experimental bedform heights and wavelengths.

1  
2  
3  
4 **Figure 18** – Conceptual model explaining variations in bed sediment flux as function of yield  
5 strength and near-bed turbulent stress. The length of the arrows to the left and above the critical  
6 shear stress line is a measure of the bed sediment flux.  
7  
8  
9

10 **Figure 19** – Schematic sedimentary logs of mixed sand-mud facies produced by decelerated high-  
11 density flows, organised according to initial suspended sediment concentrations, duration of post-  
12 deceleration steady flow, and deceleration rate. Text in red boxes summarises principal facies  
13 types (flat, stratified, structureless) and formation mechanism. Text in green boxes summarises  
14 possible types of deceleration. See main text for details. C = concentration.  
15  
16  
17  
18

19  
20 **Figure 20** – Conceptual model for segregation and mixing of particle size fractions in mixed  
21 cohesive sediment flows and their sedimentary facies, based on the inferred turbulent and  
22 cohesive carrying capacity of flows with different suspended clay concentration. Total grain support  
23 (thick line) is assumed to be equal to the sum of turbulence support and cohesive support (thin  
24 lines). Turbulence support for LTPF is subdivided into the part close to the bed (thin solid black  
25 line) and the part in the overlying rigid plug (thin dashed black line); see Fig. 2.  
26  
27  
28  
29  
30

31 **Figure 21** – Schematic log of idealised hybrid event bed with inferred processes of formation of  
32 H1-H5 divisions, based on Haughton *et al.* (2009) and this study. Modified after Haughton *et al.*  
33 (2009).  
34  
35  
36  
37  
38  
39  
40  
41  
42  
43  
44  
45  
46  
47  
48  
49  
50  
51  
52  
53  
54  
55  
56  
57  
58  
59  
60

1  
2  
3  
4  
5  
6  
7  
8  
9  
10  
11  
12  
13  
14  
15  
16  
17  
18  
19  
20  
21  
22  
23  
24  
25  
26  
27  
28  
29  
30  
31  
32  
33  
34  
35  
36  
37  
38  
39  
40  
41  
42  
43  
44  
45  
46  
47

**Table 1** - Experimental parameters

Run	Duration (h)	T (° C)	C <sub>0</sub> (vol%)	C <sub>0</sub> (g L <sup>-1</sup> )	C <sub>e</sub> (vol%)	η <sup>1</sup> (Ns m <sup>-2</sup> x10 <sup>-3</sup> )	τ <sub>y</sub> <sup>1</sup> (N m <sup>-2</sup> )	h (m)	z <sub>p</sub> (m)	f(UDVP) (Hz)	U (mm s <sup>-1</sup> )	U <sub>max</sub> (mm s <sup>-1</sup> )	Fr (-)	Re <sup>1</sup> (-)	Slope x10 <sup>-3</sup>	Flow phase
1	2.85	19.3	0.2	5.2	0.04	1.006	0.000	0.151	0.151	115	465	566	0.38	69939	1.38	TF
2	2.67	19.9	1.1	28.6	0.75	1.106	0.002	0.150	0.150	115	453	573	0.37	62434	1.38	TETF
3	2.52	19.9	1.7	44.2	1.5	1.219	0.006	0.151	0.151	115	445	539	0.37	56610	1.38	TETF
4	2.48	19.6	3.5	91.0	3.1	1.738	0.055	0.150	0.150	115	448	556	0.37	40918	1.38	TETF
5	2.50	18.9	5.1	132.6	4.6	2.389	0.170	0.149	0.149	115-116	425	534	0.35	28675	1.38	TETF
6	2.50	19.1	6.9	179.4	6.8	3.307	0.420	0.147	0.147	118	440	509	0.37	21769	1.38	LTPF
7	2.48	18.7	8.0	208.0	8.0	3.958	0.655	0.150	0.150	119-130	456	569	0.38	19530	1.38	LTPF
8	2.52	18.7	10.1	262.6	9.3	5.377	1.319	0.140	0.071	130-132	543	579	0.46	8329	1.38	UTPF
9	2.47	19.8	12.1	314.6	10.9	6.929	2.268	0.139	0.051	132	545	568	0.47	4788	0.29	QLPF
10	2.50	19.1	13.8	358.8	12.5	8.394	3.364	0.140	0.036	132	511	539	0.44	2676	1.38	QLPF
11	2.53	19.9	15.4	400.4	14.0	9.890	4.675	0.140	0.036	132	496	504	0.42	2250	1.81	QLPF
12	2.50	19.9	16.5	429.0	15.5	10.983	5.750	0.146	0.031	133	443	447	0.37	1581	2.85	QLPF
13	2.52	20.1	18.2	473.2	17.3	12.770	7.717	0.146	0.026	133	351	353	0.29	923	3.26	QLPF
14	2.55	20.5	19.2	499.2	18.2	13.877	9.060	0.150	0.019	133	447	449	0.37	800	4.24	QLPF

T = mean fluid temperature

C<sub>0</sub> = initial suspended sediment concentration (t~1 min)

C<sub>e</sub> = final depth-averaged suspended sediment concentration (t = 2.3 h)

η = dynamic viscosity

τ<sub>y</sub> = yield stress

h = flow depth

z<sub>p</sub> = height of base of plug flow region

f(UDVP) = (range of) frequency of velocity data

U = depth-averaged velocity

<sup>1</sup> This parameter is calculated using C<sub>0</sub>.

U<sub>max</sub> = maximum velocity in vertical profile

Fr = Froude number

Re = flow Reynolds number after Liu & Mei (1990)

TF = turbulent flow

TETF = turbulence-enhanced transitional flow

LTPPF = lower-phase transitional plug flow;

UTPF = upper-phase transitional plug flow

QLPF = quasi-laminar plug flow

**Table 2** - Comparison of equilibrium ripple dimensions

<b>Source</b>	<b>Equilibrium ripple height (mm)</b>	<b>Equilibrium ripple wavelength (mm)</b>
This study, TF	13.0	109.8
Baas (1993) predictor	14.3	115.9
Baas (1994) for $D_{50}=0.095$ mm	13.1	115.7
Raudkivi (1997) predictor	14.1	103.0
This study, LTPF	18.3	203.2
Baas (1993) predictor, upper limit (0.7 mm sand)	17.5	185.3
Raudkivi (1997) predictor, upper limit (0.7 mm sand)	17.4	216.2

1  
2  
3  
4  
5  
6  
7  
8  
9  
10  
11  
12  
13  
14  
15  
16  
17  
18  
19  
20  
21  
22  
23  
24  
25  
26  
27  
28  
29  
30  
31  
32  
33  
34  
35  
36  
37  
38  
39  
40  
41  
42  
43  
44  
45  
46  
47  
48  
49  
50  
51  
52  
53  
54  
55  
56  
57  
58  
59  
60

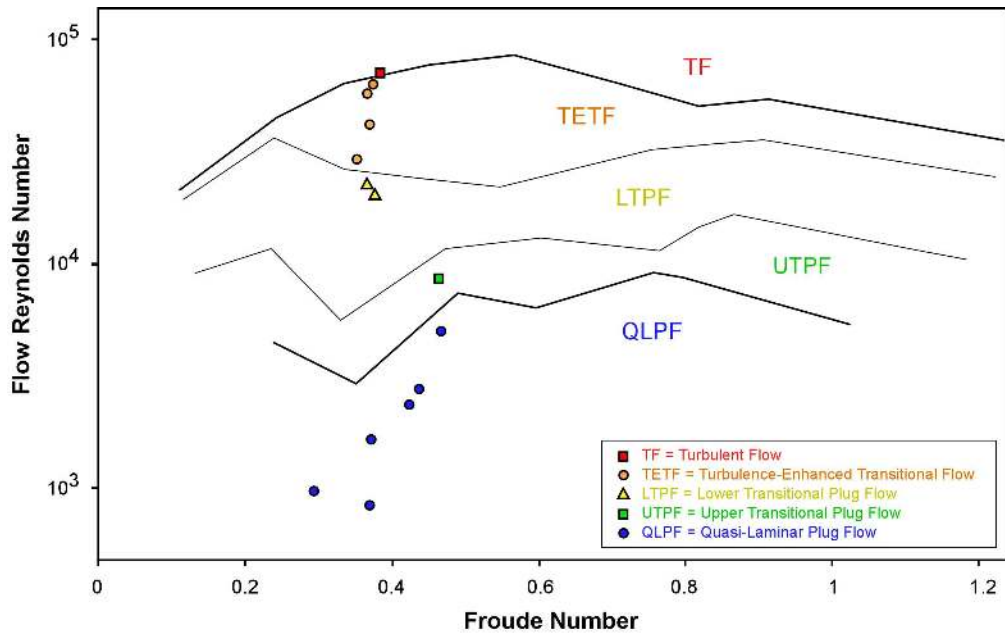


Figure 1 – Clay flow phase diagram of Baas et al. (2009). The coloured symbols denote flows investigated in the present paper.  
180x112mm (300 x 300 DPI)

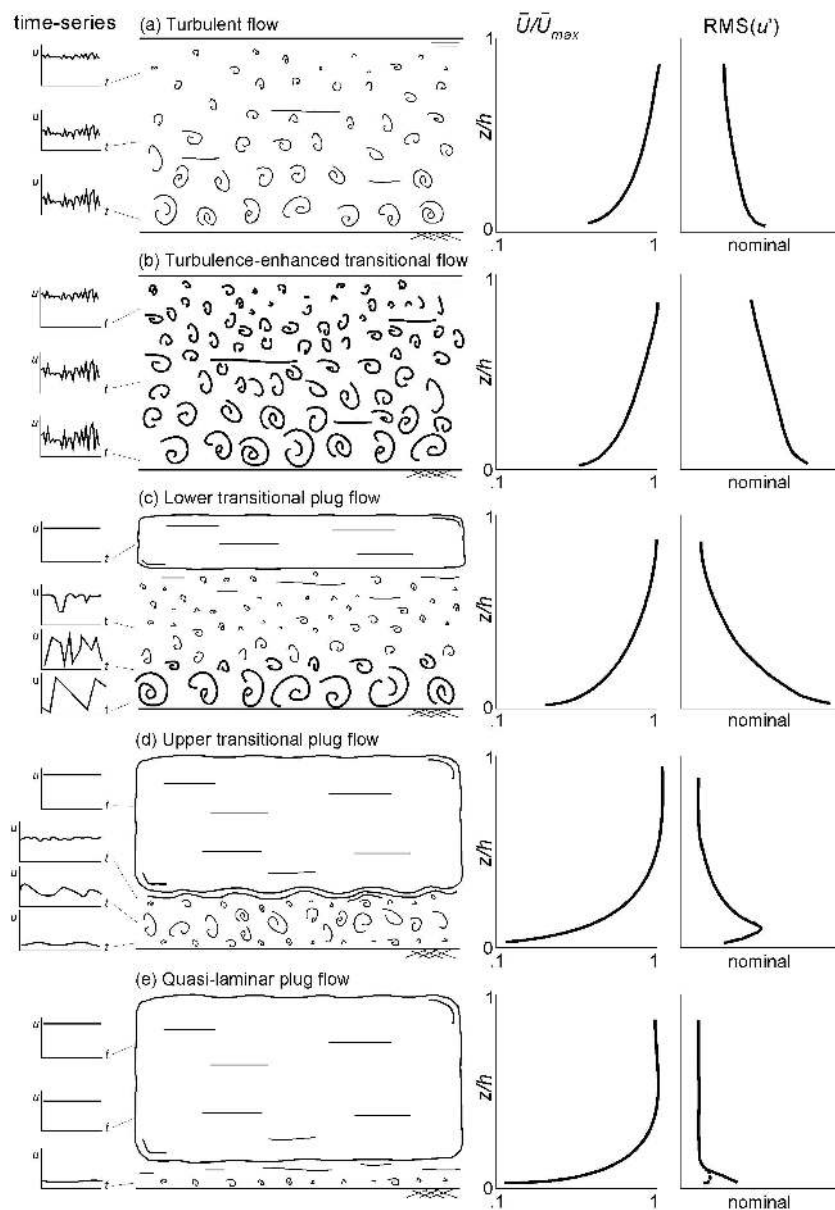


Figure 2 – Schematic models of turbulent, transitional and quasi-laminar clay flows over a smooth, flat bed. The graphs to the left of the models denote characteristic velocity time series at various heights in the flows. The graphs to the right of the models represent characteristic vertical profiles of dimensionless downstream velocity ( $\bar{U}/\bar{U}_{max}$ ) and root-mean-square of downstream velocity ( $RMS(u')$ ). Modified after Baas et al. (2009).

194x280mm (300 x 300 DPI)



1  
2  
3  
4  
5  
6  
7  
8  
9  
10  
11  
12  
13  
14  
15  
16  
17  
18  
19  
20  
21  
22  
23  
24  
25  
26  
27  
28  
29  
30  
31  
32  
33  
34  
35  
36  
37  
38  
39  
40  
41  
42  
43  
44  
45  
46  
47  
48  
49  
50  
51  
52  
53  
54  
55  
56  
57  
58  
59  
60

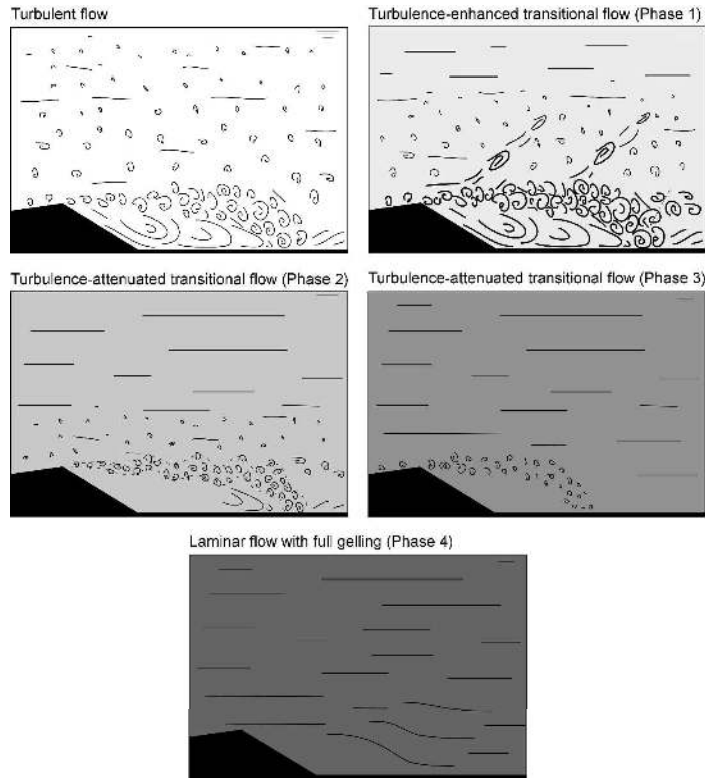


Figure 3 - Conceptual models showing the changing dynamics of flow in the leeside of a fixed, flow-transverse bedform, as a function of increasing clay concentration. Modified after Baas & Best (2008).  
320x247mm (300 x 300 DPI)

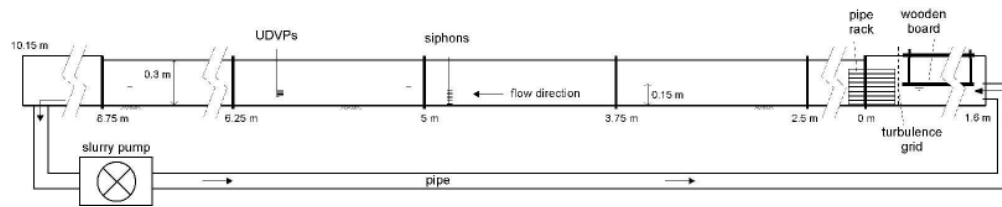


Figure 4 – Schematic diagram of the experimental set-up. UDVP = Ultrasonic Doppler Velocity Profilers.  
274x54mm (300 x 300 DPI)

1  
2  
3  
4  
5  
6  
7  
8  
9  
10  
11  
12  
13  
14  
15  
16  
17  
18  
19  
20  
21  
22  
23  
24  
25  
26  
27  
28  
29  
30  
31  
32  
33  
34  
35  
36  
37  
38  
39  
40  
41  
42  
43  
44  
45  
46  
47  
48  
49  
50  
51  
52  
53  
54  
55  
56  
57  
58  
59  
60

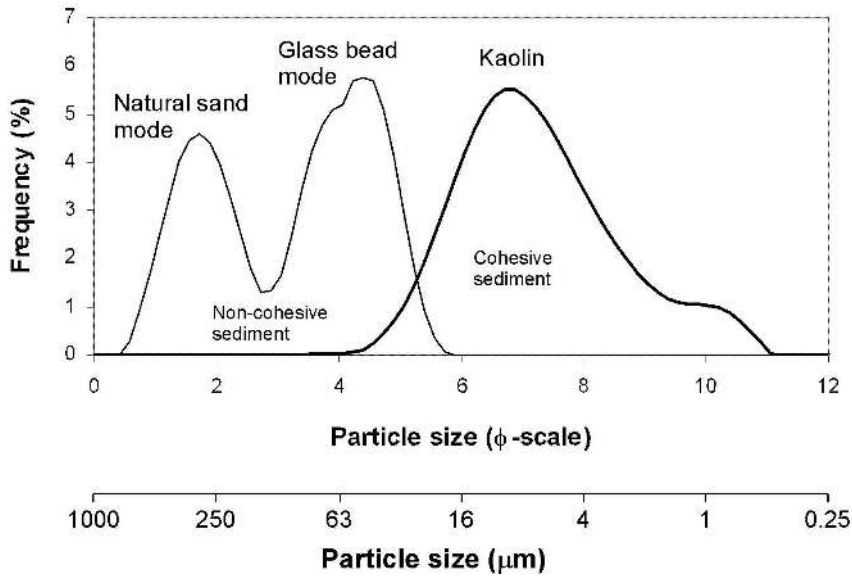


Figure 5 – Grain-size distribution curves of the cohesive and non-cohesive fractions used in the experiments. The frequencies for both fractions add up to 100%. The size class width is  $1/6\phi$ . The non-cohesive fraction was prepared by mixing two types of spherical glass beads ( $D_{50}=0.044$  mm and  $D_{50}=0.084$  mm) with two types of natural medium sand ( $D_{50}=0.283$  mm and  $D_{50}=0.310$  mm) in order to produce a sediment with a wide range of grain sizes.

148x89mm (300 x 300 DPI)

1  
2  
3  
4  
5  
6  
7  
8  
9  
10  
11  
12  
13  
14  
15  
16  
17  
18  
19  
20  
21  
22  
23  
24  
25  
26  
27  
28  
29  
30  
31  
32  
33  
34  
35  
36  
37  
38  
39  
40  
41  
42  
43  
44  
45  
46  
47  
48  
49  
50  
51  
52  
53  
54  
55  
56  
57  
58  
59  
60

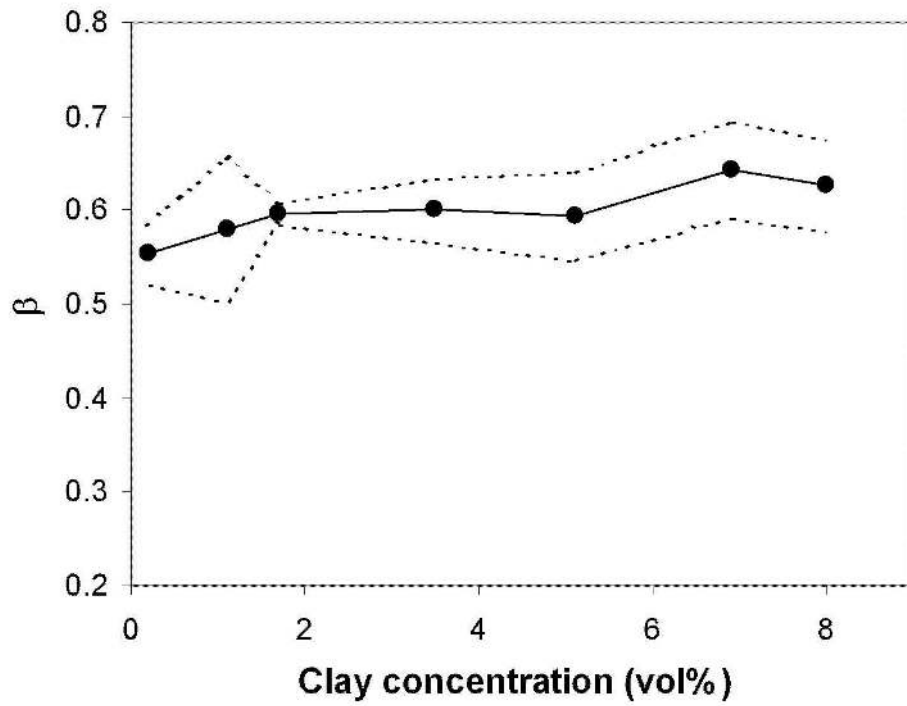


Figure 6 - Initial clay concentration plotted against  $\beta$  that is used in Eq. 10. The dashed lines indicate one standard deviation around the mean.  
115x88mm (300 x 300 DPI)

1  
2  
3  
4  
5  
6  
7  
8  
9  
10  
11  
12  
13  
14  
15  
16  
17  
18  
19  
20  
21  
22  
23  
24  
25  
26  
27  
28  
29  
30  
31  
32  
33  
34  
35  
36  
37  
38  
39  
40  
41  
42  
43  
44  
45  
46  
47  
48  
49  
50  
51  
52  
53  
54  
55  
56  
57  
58  
59  
60

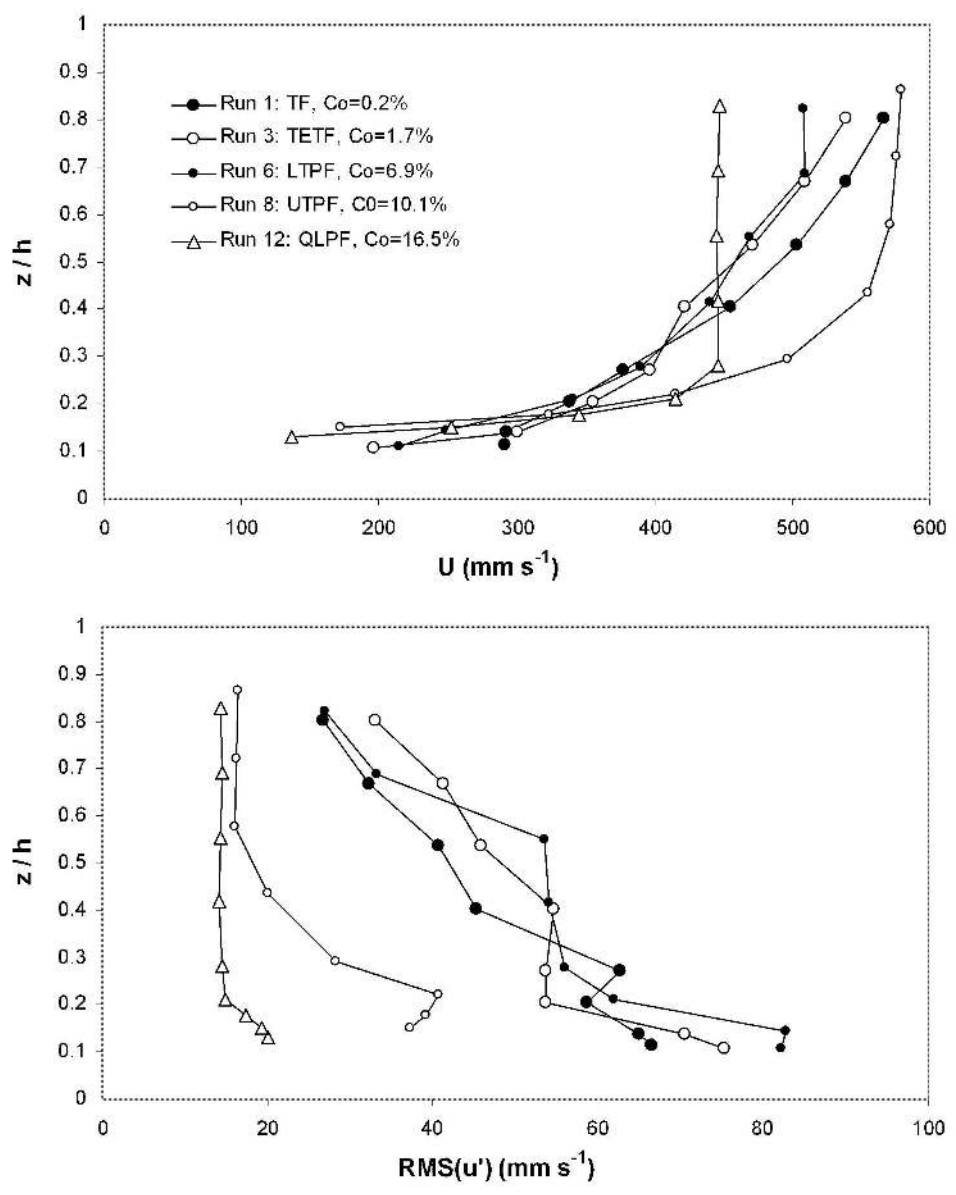


Figure 7 – Vertical profiles of time-averaged downstream flow velocity (top) and the root-mean-square of downstream velocity (bottom) for selected experimental runs.  
158x197mm (300 x 300 DPI)

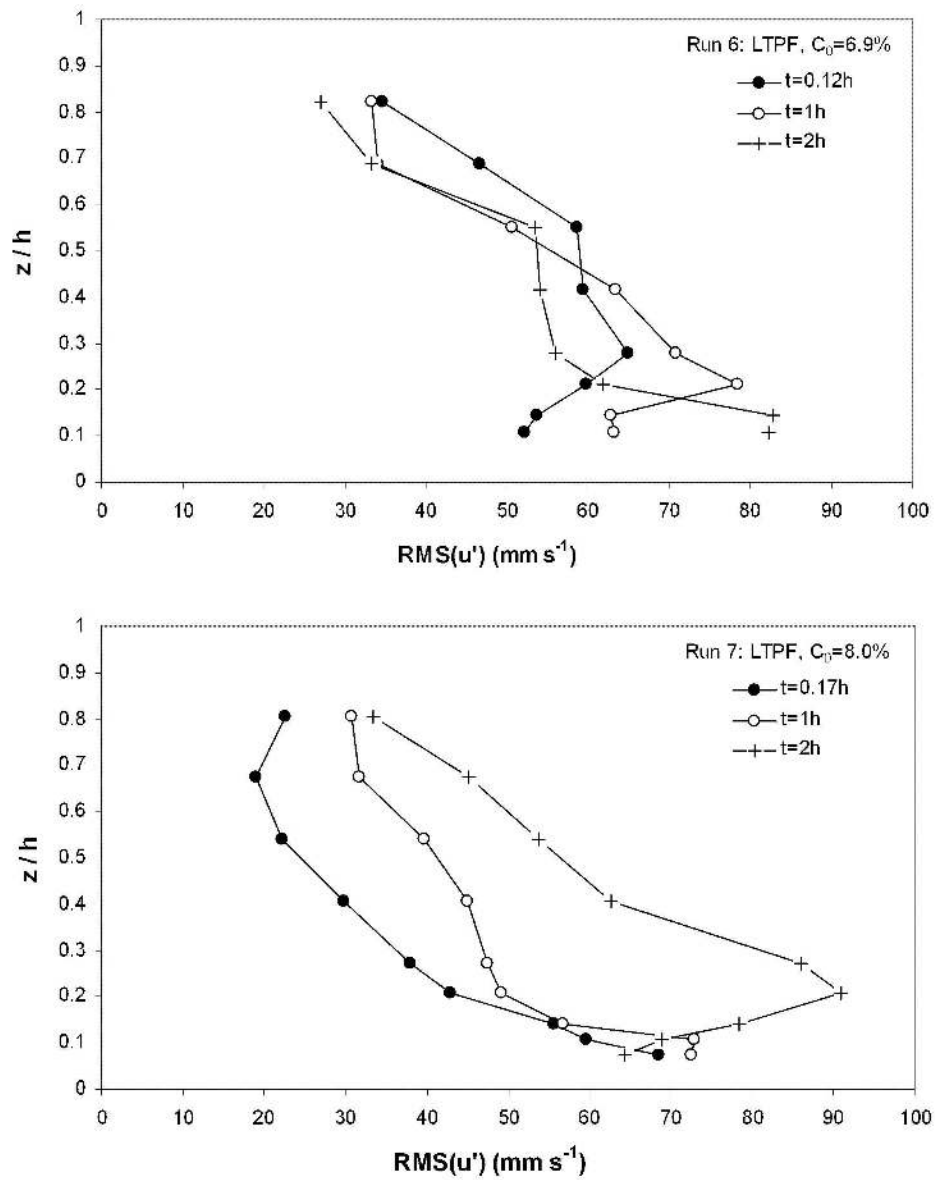


Figure 8 - Vertical profiles of the root-mean-square of downstream velocity for lower transitional plug flows. Note that RMS( $u'$ )-values change with time.  
159x201mm (300 x 300 DPI)

1  
2  
3  
4  
5  
6  
7  
8  
9  
10  
11  
12  
13  
14  
15  
16  
17  
18  
19  
20  
21  
22  
23  
24  
25  
26  
27  
28  
29  
30  
31  
32  
33  
34  
35  
36  
37  
38  
39  
40  
41  
42  
43  
44  
45  
46  
47  
48  
49  
50  
51  
52  
53  
54  
55  
56  
57  
58  
59  
60

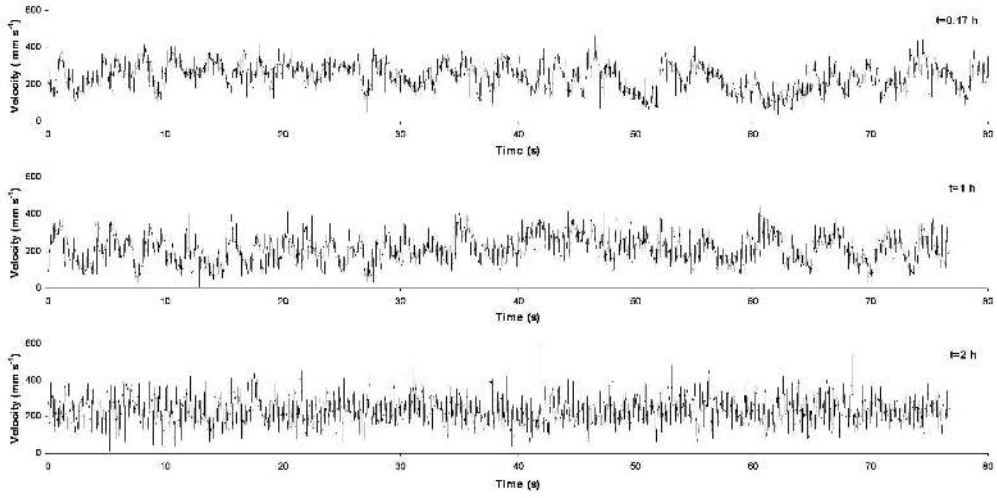


Figure 9 – Time series of downstream velocity at ~6 mm above the bed in Run 7 (C0=8.0%) at 3 different points in time. Note the pronounced saw-tooth shaped velocity fluctuations at t=0.17 h, and to a lesser degree at t=1 h  
291x145mm (300 x 300 DPI)

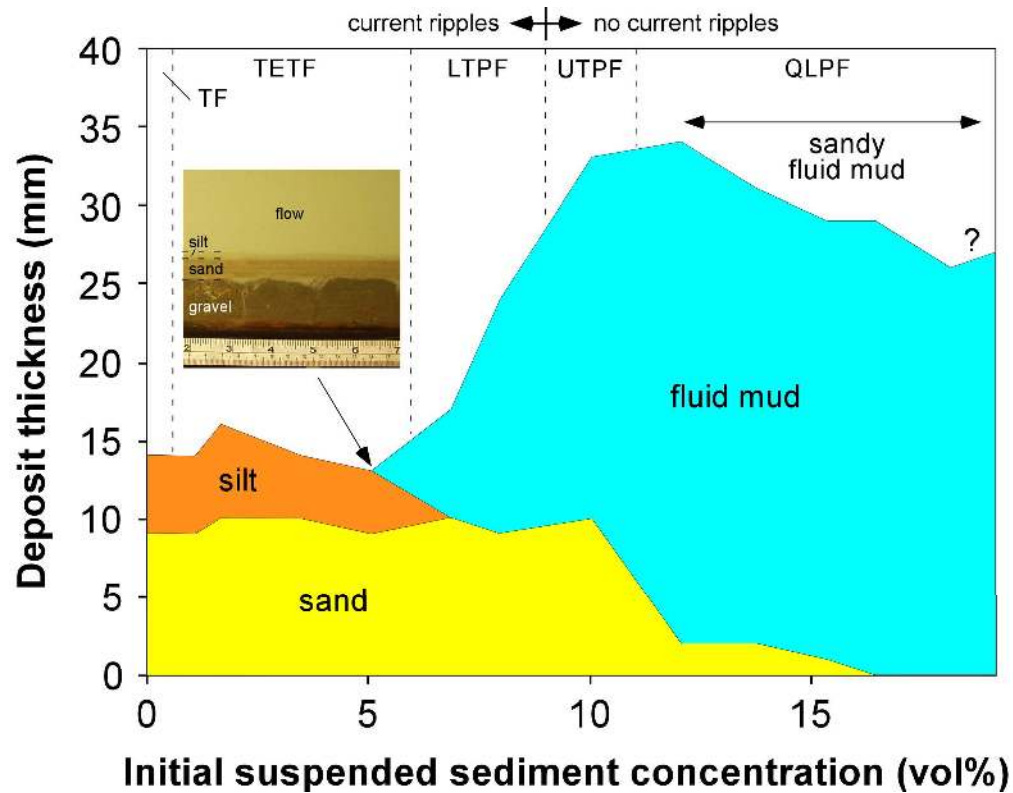


Figure 10 – Thickness and textural features of deposits formed after rapid flow deceleration and just before bedform development commenced. The question mark denotes estimated thickness, because of difficulties in recognising the flow-bed interface. Scale on photograph is in inches (top) and centimetres (bottom). The information above the graph refers to the boundary concentration for bedform development that occurred after the formation of the initial flat bed.  
177x139mm (300 x 300 DPI)



1  
2  
3  
4  
5  
6  
7  
8  
9  
10  
11  
12  
13  
14  
15  
16  
17  
18  
19  
20  
21  
22  
23  
24  
25  
26  
27  
28  
29  
30  
31  
32  
33  
34  
35  
36  
37  
38  
39  
40  
41  
42  
43  
44  
45  
46  
47  
48  
49  
50  
51  
52  
53  
54  
55  
56  
57  
58  
59  
60

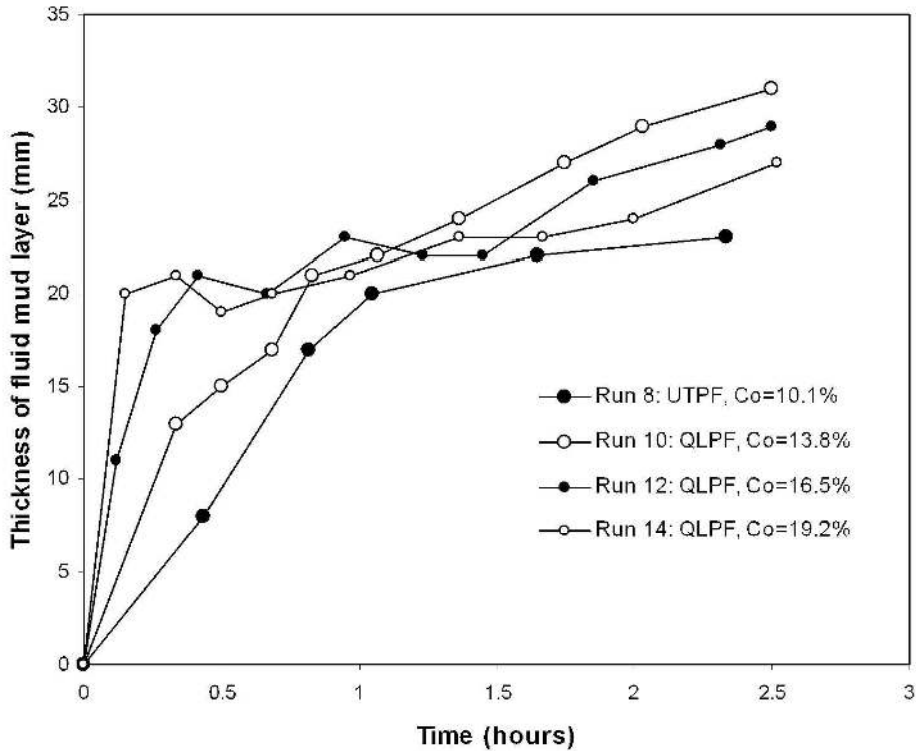


Figure 11 – Temporal development of fluid mud layer thickness in the upper transitional plug flow and the quasi-laminar plug flows.  
139x114mm (300 x 300 DPI)

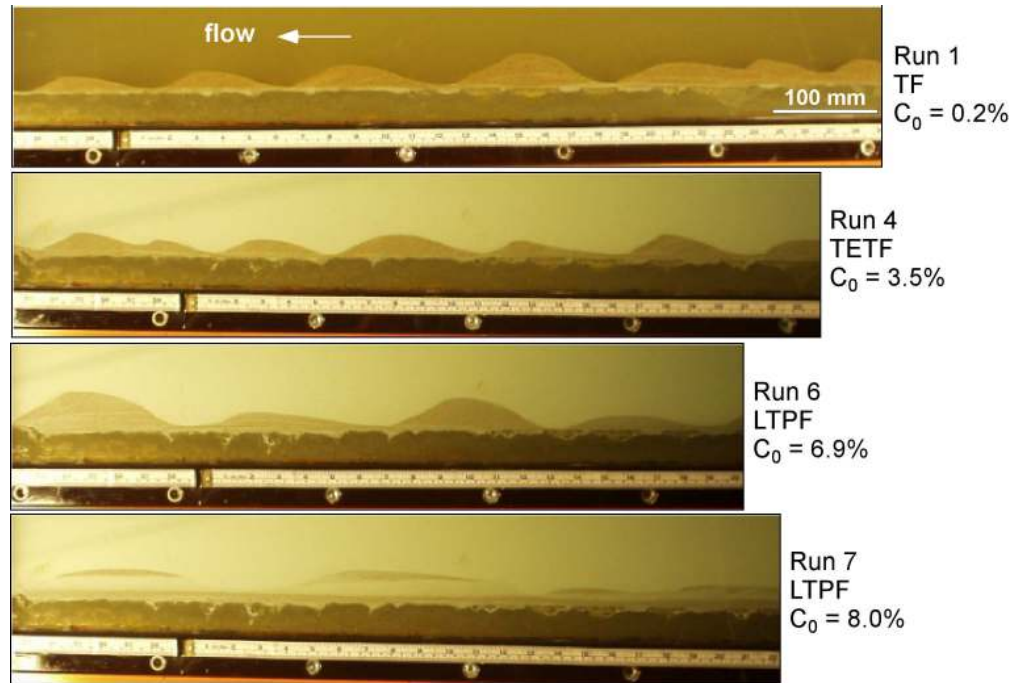


Figure 12 – Sidewall photographs of final bedforms in selected experimental runs. Note the increase in ripple height and wavelength with increasing suspended sediment concentration and the muddy character of the ripple cores in Run 7 ( $C_0=8.0\%$ , shown by light colours).

193x153mm (300 x 300 DPI)

1  
2  
3  
4  
5  
6  
7  
8  
9  
10  
11  
12  
13  
14  
15  
16  
17  
18  
19  
20  
21  
22  
23  
24  
25  
26  
27  
28  
29  
30  
31  
32  
33  
34  
35  
36  
37  
38  
39  
40  
41  
42  
43  
44  
45  
46  
47  
48  
49  
50  
51  
52  
53  
54  
55  
56  
57  
58  
59  
60

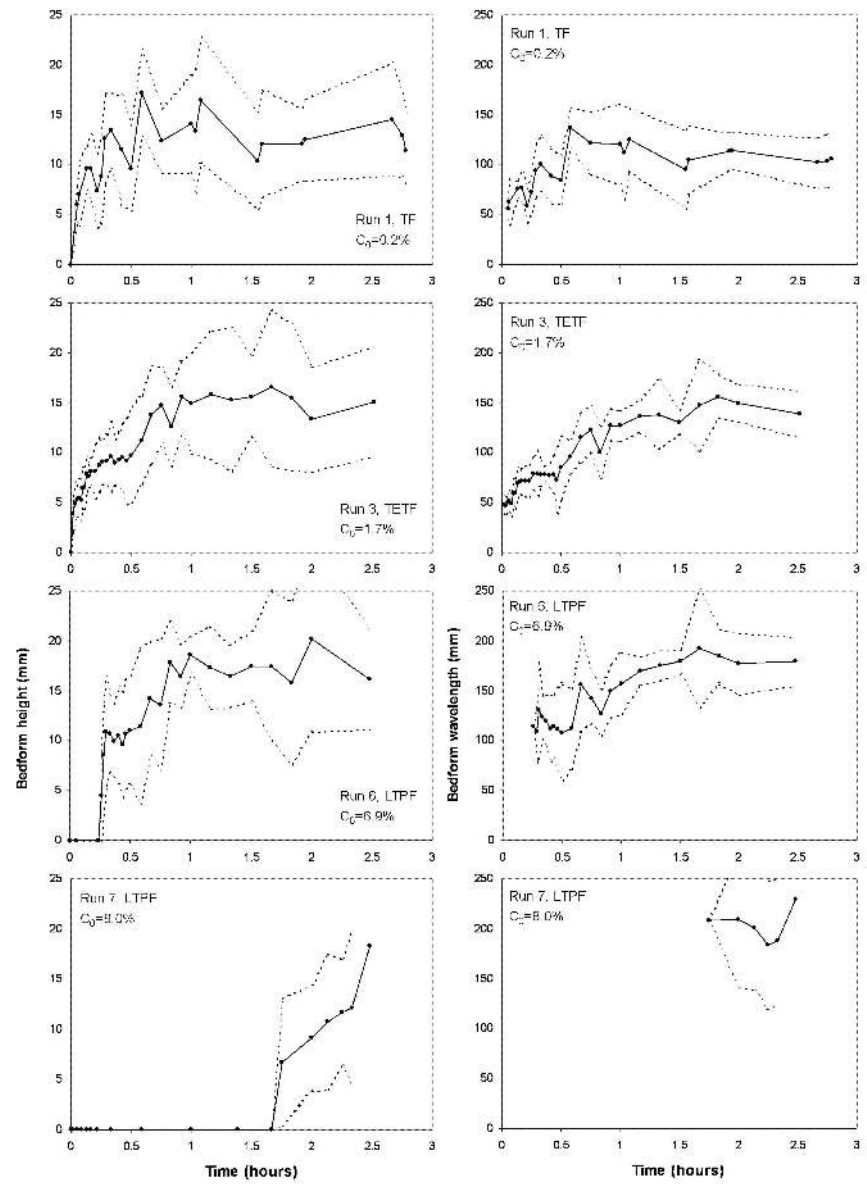


Figure 13 – Bedform height and wavelength development curves for selected runs in one turbulent flow and three lower transitional plug flows. Dashed lines indicate one standard deviation around the mean.  
210x288mm (300 x 300 DPI)

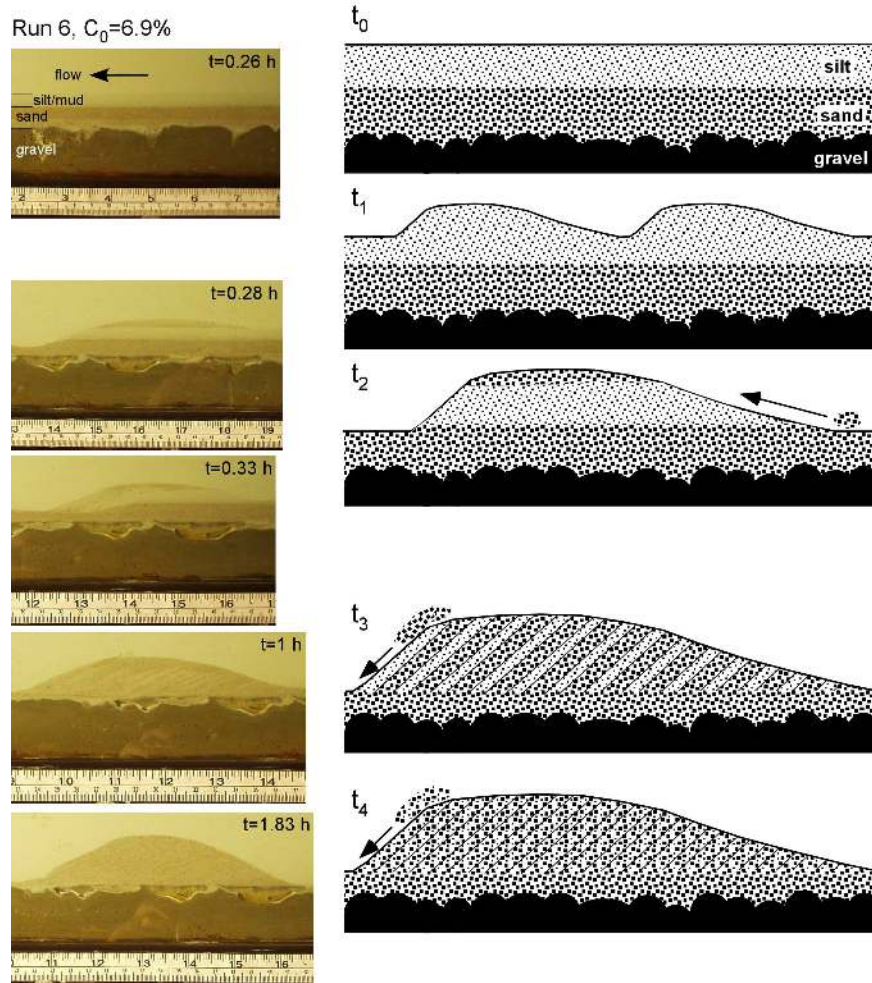


Figure 14 – Photographs and schematic drawings of bedforms in progressive stages of development starting from an initial flat bed. The drawings are valid for TF, TETF and LTPF. The photographs are from Run 6 ( $C_0=6.9\%$ ), in which the fine-grained top of the initial flat bed (at  $t=0.26$  h) was more cohesive than in runs with lower suspended clay concentrations. Scale on photographs is in inches (top) and centimetres (bottom).  
191x188mm (300 x 300 DPI)

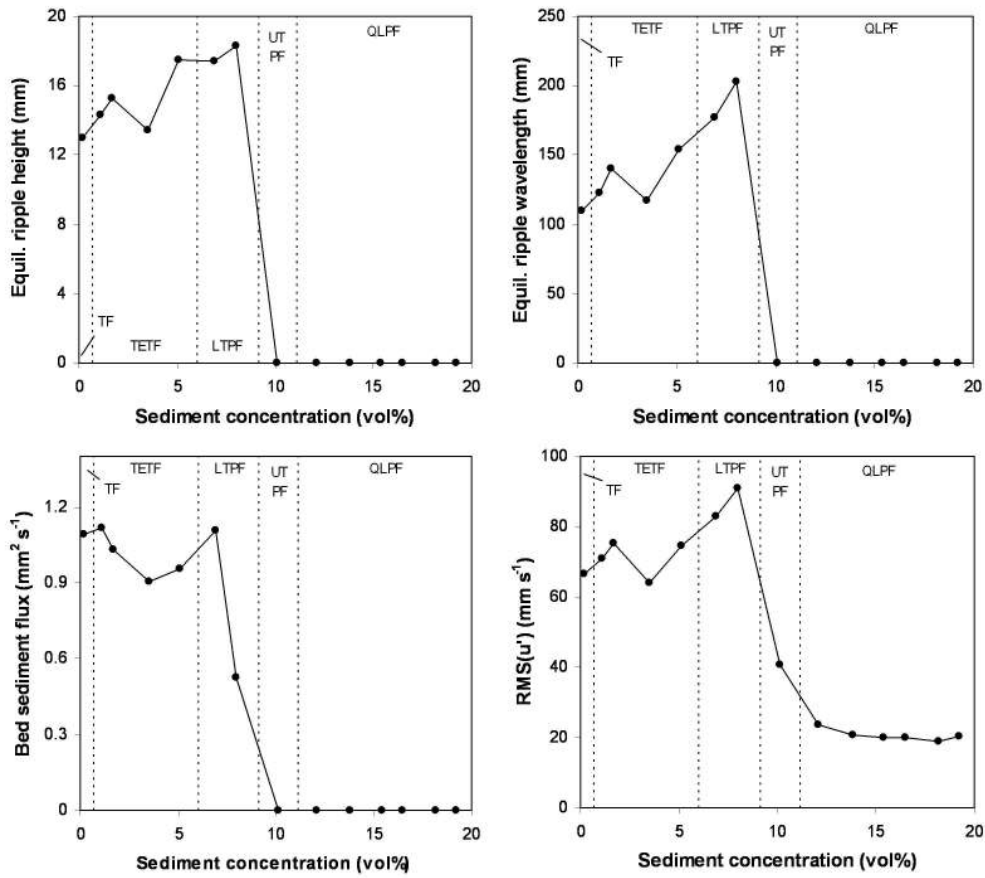


Figure 15 - Relationships between initial suspended sediment concentration and (a) equilibrium bedform height, (b) equilibrium bedform wavelength, (c) bed sediment flux and (d) RMS( $u'$ ).  
201x179mm (300 x 300 DPI)

1  
2  
3  
4  
5  
6  
7  
8  
9  
10  
11  
12  
13  
14  
15  
16  
17  
18  
19  
20  
21  
22  
23  
24  
25  
26  
27  
28  
29  
30  
31  
32  
33  
34  
35  
36  
37  
38  
39  
40  
41  
42  
43  
44  
45  
46  
47  
48  
49  
50  
51  
52  
53  
54  
55  
56  
57  
58  
59  
60

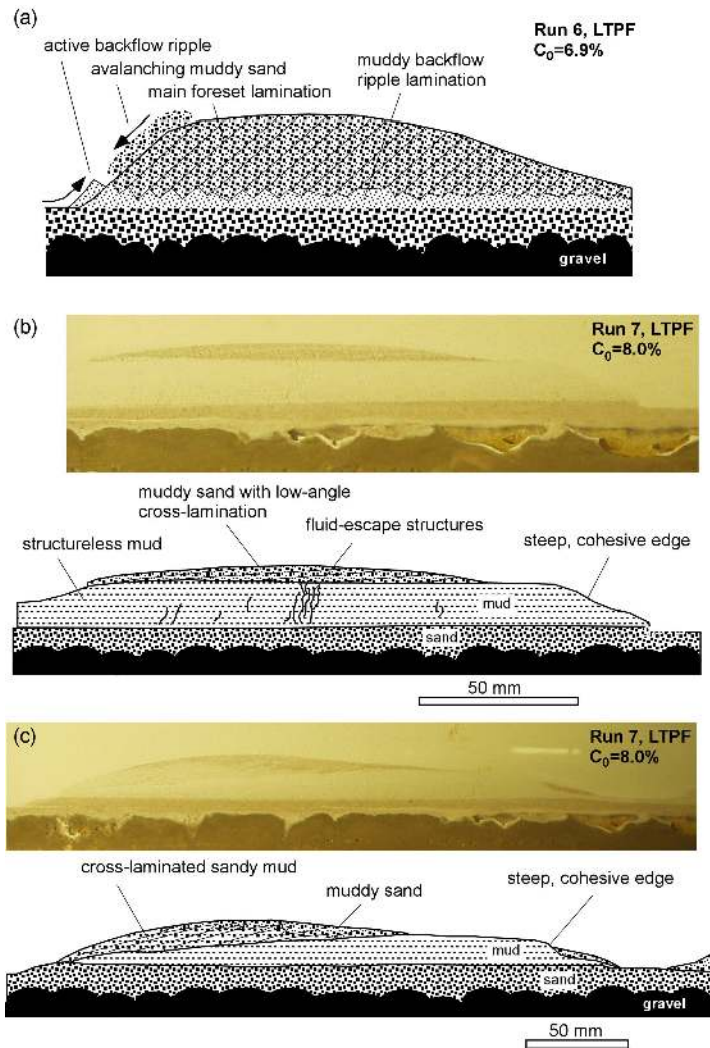


Figure 16 – (a) Schematic drawing of a current ripple with prominent backflow ripples in Run 6 ( $C_0=6.9\%$ ). This ripple corresponds to the bedform at  $t_4$  in Fig. 14. Not to scale. (b) Photograph and labelled drawing of characteristic bedforms in Run 7 ( $C_0=8.0\%$ ) at  $t=1.08$  h. (c) Photograph and labelled drawing of characteristic bedforms in Run 7 at  $t=1.5$  h. Note that the core of firm mud in (b) and (c) affects bedform properties. See text for details.  
240x250mm (300 x 300 DPI)

1  
2  
3  
4  
5  
6  
7  
8  
9  
10  
11  
12  
13  
14  
15  
16  
17  
18  
19  
20  
21  
22  
23  
24  
25  
26  
27  
28  
29  
30  
31  
32  
33  
34  
35  
36  
37  
38  
39  
40  
41  
42  
43  
44  
45  
46  
47  
48  
49  
50  
51  
52  
53  
54  
55  
56  
57  
58  
59  
60

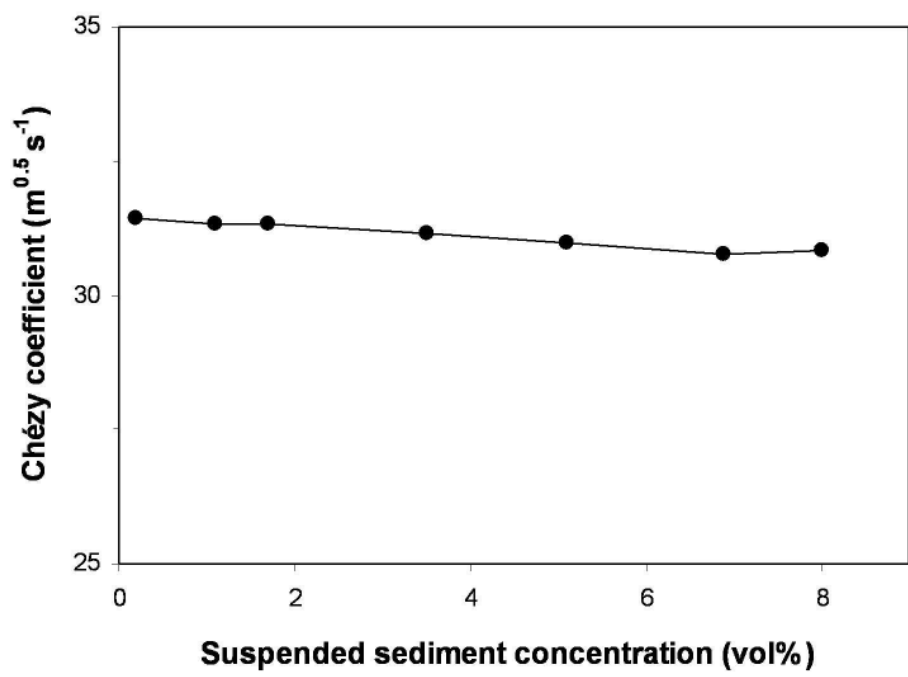


Figure 17 – Relationship between initial suspended sediment concentration and Chézy coefficient calculated for the experimental bedform heights and wavelengths.  
133x99mm (300 x 300 DPI)

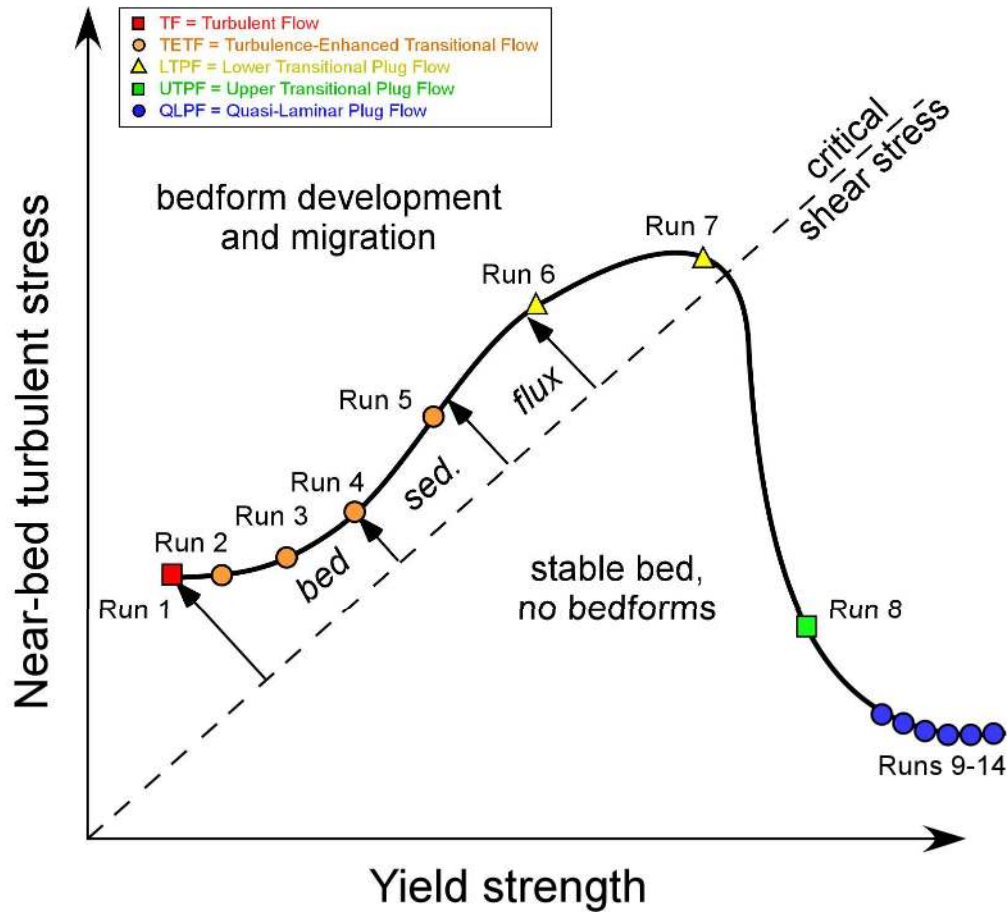


Figure 18 – Conceptual model explaining variations in bed sediment flux as function of yield strength and near-bed turbulent stress. The length of the arrows to the left and above the critical shear stress line is a measure of the bed sediment flux.  
139x125mm (300 x 300 DPI)



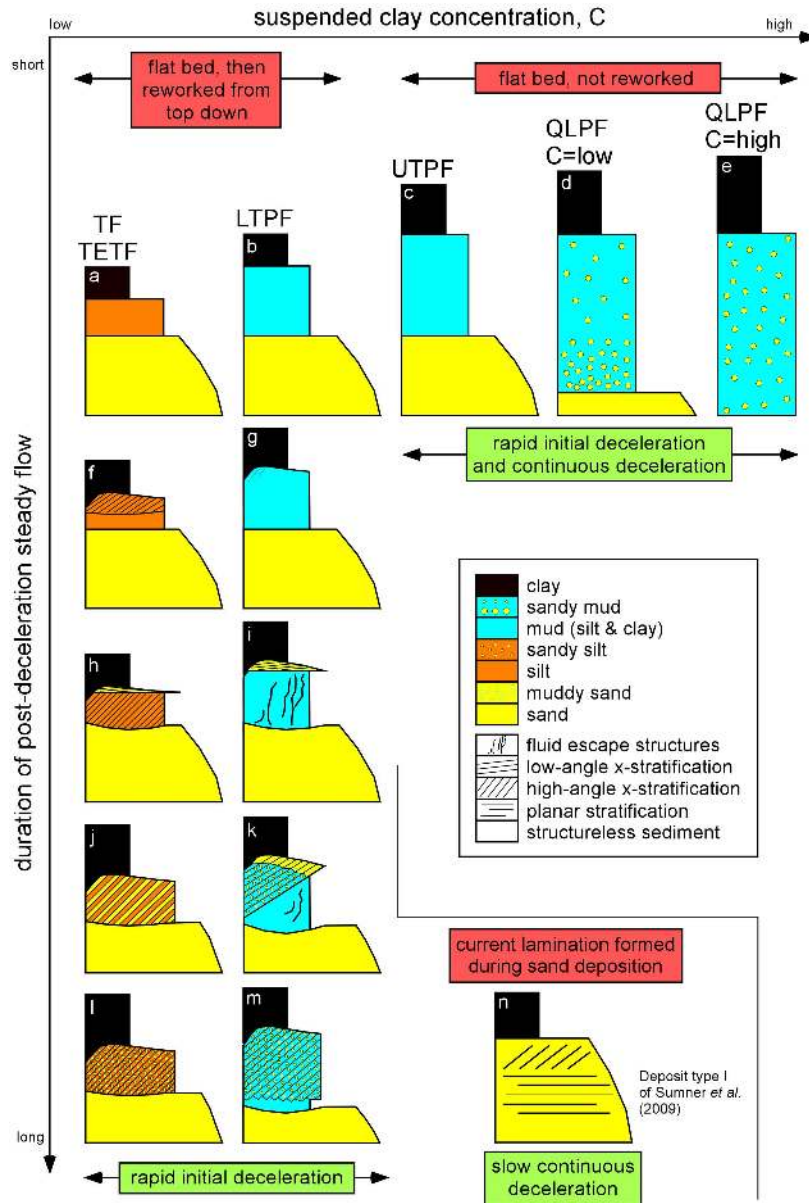


Figure 19 – Schematic sedimentary logs of mixed sand-mud facies produced by decelerated high-density flows, organised according to initial suspended sediment concentrations, duration of post-deceleration steady flow, and deceleration rate. Text in red boxes summarises principal facies types (flat, stratified, structureless) and formation mechanism. Text in green boxes summarises possible types of deceleration. See main text for details. C = concentration.  
178x263mm (300 x 300 DPI)

1  
2  
3  
4  
5  
6  
7  
8  
9  
10  
11  
12  
13  
14  
15  
16  
17  
18  
19  
20  
21  
22  
23  
24  
25  
26  
27  
28  
29  
30  
31  
32  
33  
34  
35  
36  
37  
38  
39  
40  
41  
42  
43  
44  
45  
46  
47  
48  
49  
50  
51  
52  
53  
54  
55  
56  
57  
58  
59  
60

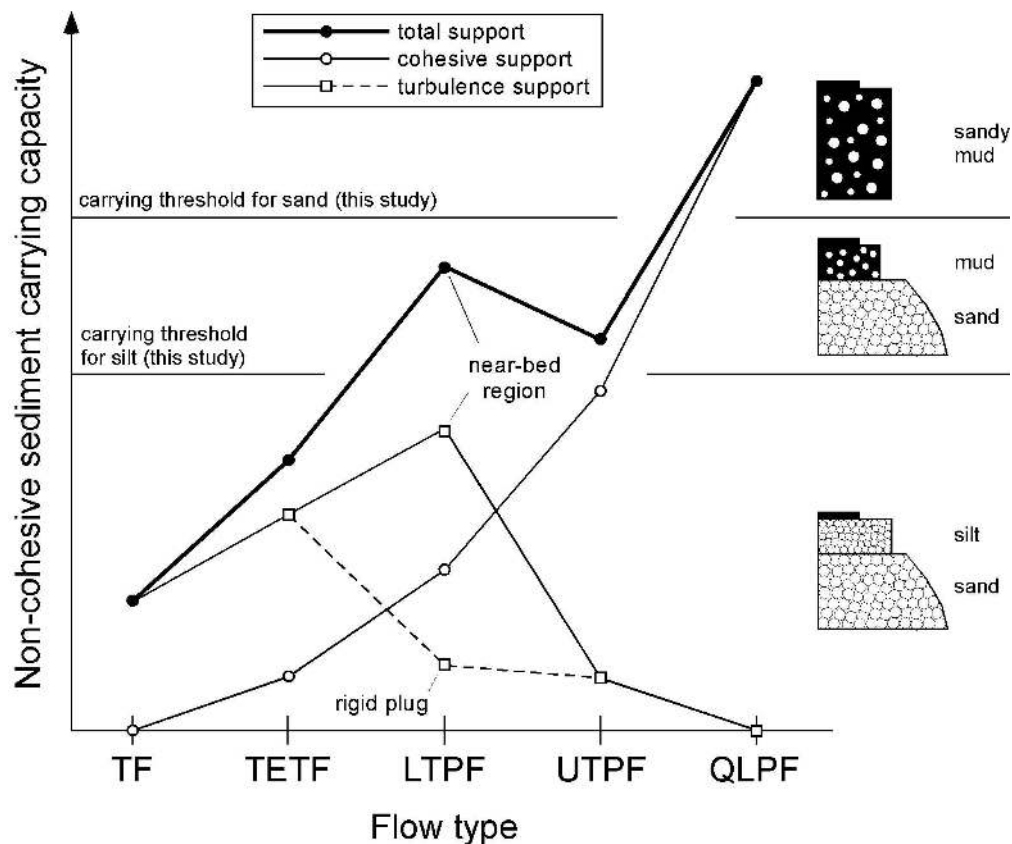


Figure 20 – Conceptual model for segregation and mixing of particle size fractions in mixed cohesive sediment flows and their sedimentary facies, based on the inferred turbulent and cohesive carrying capacity of flows with different suspended clay concentration. Total grain support (thick line) is assumed to be equal to the sum of turbulence support and cohesive support (thin lines). Turbulence support for LTPF is subdivided into the part close to the bed (thin solid black line) and the part in the overlying rigid plug (thin dashed black line); see Fig. 2.

167x140mm (300 x 300 DPI)

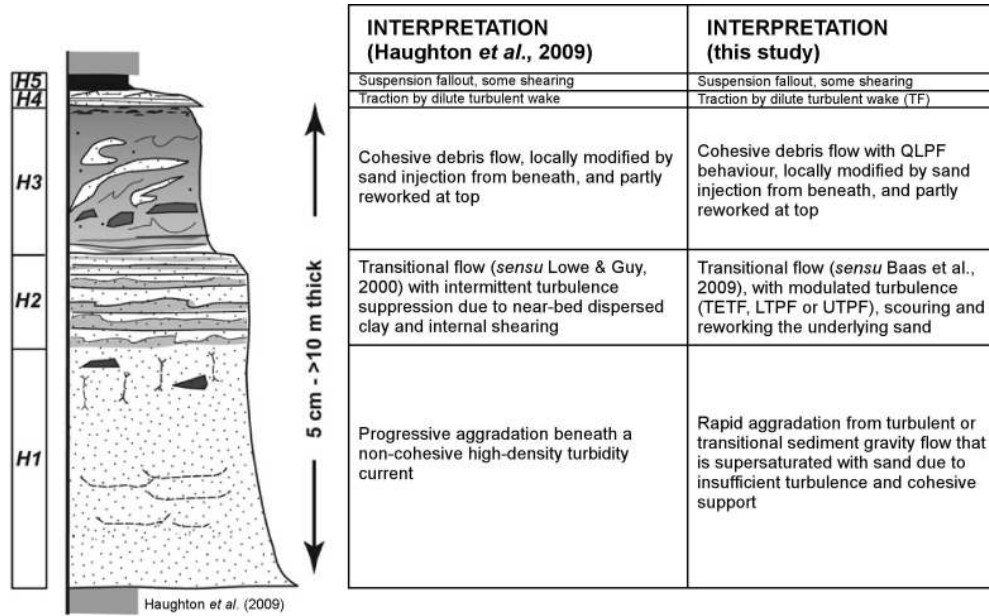


Figure 21 – Schematic log of idealised hybrid event bed with inferred processes of formation of H1-H5 divisions, based on Haughton et al. (2009) and this study. Modified after Haughton et al. (2009).  
200x124mm (300 x 300 DPI)

1  
2  
3  
4  
5  
6  
7  
8  
9  
10  
11  
12  
13  
14  
15  
16  
17  
18  
19  
20  
21  
22  
23  
24  
25  
26  
27  
28  
29  
30  
31  
32  
33  
34  
35  
36  
37  
38  
39  
40  
41  
42  
43  
44  
45  
46  
47  
48  
49  
50  
51  
52  
53  
54  
55  
56  
57  
58  
59  
60